4D forward stratigraphic modelling of the Late Quaternary Congo deep-sea fan: Role of climate/vegetation coupling in architectural evolution

Abstract

The relative impacts of autogenic and allogenic controls on the architectural evolution of deep-sea fans are not well constrained, mainly because of the difficulty in evaluating the role of each control on any specific stratigraphic pattern. This study presents four-dimensional (4D) forward stratigraphic modelling of the Late Quaternary Congo Axial Fan, which provides new insights on forcing factors of sedimentation over time. This modelling is based on a geological model describing successive sedimentary progradational/retrogradational cycles in the Congo turbidite system during the last 38 kyr. Analyses of geophysical and marine core data have suggested that the architectural cycles were controlled by changes in fluvial sediment discharge in relation to arid and humid periods in the Congo River watershed. The aims of this study were to simulate the architectural evolution of the Late Quaternary Congo Axial Fan from 210 ka to the present and investigate the factors controlling sedimentation using DionisosFlow^{TM}, a process-based stratigraphic forward modelling software. For this objective, several scenarios were tested to simulate the role of autogenic and climate forcings based on proxies recorded in marine sediments. The modelling results confirmed that climatic variations of sediment and water discharge succeeded in reproducing the timing, position, and sediment volume of basin-scale prograding/retrograding cycles. The best-fit simulations particularly emphasise the role of continental vegetation cover expansion, governed by the precession-driven West African monsoon, on the sediment flux to the deep-marine environment. This vegetation/climate coupling acts directly on the transport capacity of flow over time by controlling the magnitude of river runoff and the timing of sediment production, storage, and transfer from the continent to the ocean. Thus, our results confirm the utility of stratigraphic forward models in constraining 'source-to-sink' models for the architectural evolution of submarine fans.

Keywords: Congo; Quaternary; turbidite system; deep-sea fan; vegetation/climate coupling; sedimentary cycles; geophysical data; stratigraphic modelling; DionisosFlow^{TM}; palaeoclimate

1. Introduction

A large number of interacting autogenic (internal) and allogenic (external) factors influence the evolution of submarine fans, the largest depositional bodies on the planet. Crucial control in the position and timing of avulsions (abandonment and lateral migration of channels) along turbidite systems is associated with internal factors such as topographic compensation, sinuosity of channels, and the dynamics of currents, which favour instabilities within the channel and levee systems and emplacement of mass transport complexes (Flood and Piper, 1997; Pirmez et al., 1997; Lopez, 2001; Kneller, 2003; Maslin et al., 2006; Kolla, 2007; Labourdette and Bez, 2010; Armitage et al., 2012). In addition, several external factors affecting sedimentation in turbidite systems have also been outlined, such as eustacy (Posamentier et al., 1991; Lopez, 2001; Posamentier and Kolla, 2003; Bourget et al., 2011), intra-basinal and extra-basinal tectonic movements (Hoorn et al., 1995; Prather et al., 1998; Turakiewicz, 2004; Anka et al., 2009; Broucke et al., 2004; Sømme et al., 2009; Prather, 2020), and climate changes in the drainage basin (e.g. Milliman and Syvitski, 1992; Zabel et al., 2001; Toucanne et al., 2008; Toucanne et al., 2012; Ducassou et al., 2009; Picot et al., 2019), which are sometimes linked to orbital periodicities (Foucault et al., 1987; Weltje and de Boer, 1993; Schneider et al., 1997; Weber et al., 2003; Heard et al., 2008; Ducassou et al., 2009; Cantalejo and Pickering, 2015; Scotchman et al., 2015). In particular, several authors have highlighted the role of Milankovitch precession cycles in the variation of monsoon intensity, which inevitably impacts the sediment yield in drainage basins and thus the sediment transfer from rivers to deep-sea fans (Bengal Fan – Weber et al., 2003; Nile system – Ducassou et al., 2009; Niger Delta – Zabel et al., 2001; Congo Fan – Schneider et al., 1997; Holtvoeth et al., 2001; Caley et al., 2011; Picot et al., 2019). It is now accepted that the impact of climate changes on the sediment budget must be studied from the perspective of climate/vegetation coupling (Foley et al., 1994; Kutzbach et al., 1996; Brovkin et al., 1998; Ganopolski et al., 1998; Claussen et al., 1999), as the extent and density of vegetation partly control sediment production on land through the balance between mechanical and

chemical weathering of soils (e.g. Renard et al., 1997). However, if the link between climate/vegetation coupling and sediment transfer to the ocean is inferred from proxies in marine sediment cores, the response in terms of the architectural evolution of the submarine fan is not well constrained. More specifically, the respective roles of the climate-driven variations of water discharge and sediment flux cannot be investigated without individualising the factors responsible for specific stratigraphic architecture in deep-marine basins, both in time and space. With this objective, recent studies have moved toward forward modelling; more specifically, slope- and water-driven diffusion process-based simulations have already shown their usefulness in investigating sedimentary transfers in continental shelf and deep-water systems using short computation times (Kaufman et al., 1991; Granjeon and Joseph, 1999; Steckler et al., 1999; Rabineau et al., 2005; Lai and Capart, 2007; Mitchell and Huthnance, 2008; Alzaga-Ruiz et al., 2009; Csato et al., 2013; Seard et al., 2013; Gvirtzman et al., 2014; Leroux et al., 2014; Deville et al., 2015). However, investigations of the architecture of turbidite systems on abyssal plains using diffusion models at a 'source-to-sink' scale are very recent (Deville et al., 2015; Hawie et al., 2018; Burgress et al., 2019; Hawie et al., 2019; Sangster et al., 2019) and need to be enriched and confirmed by additional studies.

In this sense, the Late Quaternary Congo Fan is a good candidate to test diffusion process-based models as the large geophysical and geological database available for this fan may help to constrain the potential effects of continental climatic changes on the growth patterns of the fan over time. This fan was the subject of nine oceanographic cruises between 1992 and 2011, led by Ifremer and the University of Brest in collaboration with Total, with a total acquisition of 16,000 km of seismic lines, chirp sonar bottom profiles, multi-beam bathymetric lines, and 172 marine cores. Analysis of this database revealed successive progradational/retrogradational cycles of depocentres over time since at least 210 ka (Picot et al., 2016). Picot et al. (2019) demonstrated that the growth pattern of the fan since 38 ka is potentially linked to changes in water and sediment discharge to the

ocean in relation to the timing of variations of monsoon intensity. Beyond 38 ka and up to 210 ka, there are some uncertainties in the chronostratigraphic calibration, partly because of incomplete geophysical coverage and inherent difficulties in accurately dating sediments in turbiditic environments. If the variation in monsoon intensity controlled the sediment supply over time for the last 38 kyr, other mechanisms may be involved at longer time scales. This work constitutes the first attempt to model the three-dimensional (3D) architectural evolution of the Late Quaternary Congo Fan using DionisosFlow^{TM}, a process-based diffusion forward stratigraphic model (Granjeon, 1997; Granjeon and Joseph, 1999). The main objective of this study was to demonstrate the possible correspondence between the stratigraphic architecture of a deep-sea fan produced using diffusion-based stratigraphic forward modelling software and a real-world case study through an inversion process. Our method is based on: (i) determination of the simulation inputs inferred from the seismic and geological data, and demonstration of the relevance of the slope- and water-driven diffusion model to simulate the turbidite environment, and (ii) validation of the model against recent geological mapping and the conceptual model proposed by Picot et al. (2019) to identify the relative impacts of internal and external factors on sediment transport and distribution in the turbidite environment. This study helps to build confidence in the use of diffusion process-based stratigraphic forward models for construction of static economic reservoirs (for energy, storage, etc.) and understanding the distribution of terrestrial pollutants (e.g. microplastics; Kane et al., 2019) conveyed by rivers to the ocean.

2. The Congo sedimentary system

2.1. The Congo River

The Congo Fan is located on the Congo–Angola margin (Fig. 1). Its formation was initiated just after a major submarine erosion event that occurred on the outer shelf during the Early

Oligocene (Nze Abeigne, 1997; Lavier et al., 2000; Lavier et al., 2001). At this time, a combination of continental uplift, associated global sea-level fall, and the establishment of a humid climate in the Congo River watershed led to a considerable increase in sediment supply to the Atlantic Ocean (Droz et al., 1996; Anka and Séranne, 2004). The low degree of crystallinity of smectite confirms that at least 95% of the deposited sediment in the submarine fan is supplied by the Congo River, and that a negligible component may be associated with oceanic currents or trade winds (Gingele et al., 1998). The Congo River is currently one of the largest river systems in the world, with a length of 4,370 km draining a catchment area of 3.7×10^6 km² (Van Weering and Van Iperen, 1984). The Congo River watershed receives $5{,}530 \times 10^9$ m^3 of rainfall annually, of which $1{,}350 \times 10^9$ m^3 was estimated by Moguedet (1988) to feed the ocean, representing 80% of the fluvial supply in the Gulf of Guinea and 4% of the world's carbon input to the ocean (Martins and Probst, 1991; Rabouille et al., 2019). At present, its average flow of 41,000 m^3/s (Laraque et al., 1993; Laraque et al., 2009; Laraque et al., 2013; Alsdorf et al., 2016) ranks the Congo River second to the Amazon River globally. The sediment flux is comparatively low (ranked 17^{th} worldwide) with a mean value of 86 Mt/yr (Fig. 1), including 33 Mt/yr of total suspended sediments and 53 Mt/yr of total dissolved matter (Laraque et al., 2009, 2013). This weak sediment load is probably related to the present climate of West Africa, where chemical erosion and vegetation cover are widespread because of warm and humid conditions, even though mechanical erosion still prevails (Summerfield and Hulton, 1994; Gaillardet et al., 1995). The low mean slope gradient of the Congo River watershed has led to the formation of several lakes and pools, which favour trapping of coarse-grained materials in the central part of the basin (Molliex et al., 2019) and in the estuary in the form of prograding sandy river mouth bars (Moguedet, 1988; Wefer et al., 1998). Nevertheless, the real proportion of sediment reaching the submarine canyon remains unknown. It is assumed that between one-third and two-thirds of the sediment supply conveyed by the river currently reaches the

oceanic domain (Moguedet, 1988), but the lack of direct measurements in the estuary does not allow confirmation of this proportion.

2.2. General architecture of the Late Quaternary Congo Fan since 210 ka

The Late Quaternary Congo Fan can be divided into three main entities; from oldest to youngest, these are—the Northern Fan (780 to 540 ka), the Southern Fan (540 to 210 ka), and the Axial Fan (210 ka to present) (Droz et al., 2003). Extensive geophysical surveys carried out from 1992 to 2011 (see the legend of Fig. 1 for references to cruises) provided an accurate map of the Late Quaternary Congo turbidite system (Fig. 2a). An integrated analysis of architectural parameters (channel length and distance of avulsion points from the source point) of the Congo Fan revealed organisation into prograding/retrograding architectural cycles (Fig. 2b) (Marsset et al., 2009; Picot et al., 2016). The cycles belonging to the Axial Fan were placed into an accurate chronostratigraphic framework based on sediment dating (Picot et al., 2019)—cycle A from 210 to 130–110 ka, cycle B from 130–110 to 80–70 ka, cycle C from 80–70 to 11 ka, and cycle D, which is still active, from 11 ka to the present. The entire volume of the Axial Fan has been evaluated to be 7,500 km^3 (this study).

2.3. Conceptual model of Congo Fan architecture since 38 ka

According to Picot et al. (2016), the architectural evolution of the Axial Fan shows that internal control by topographic compensation is omnipresent and linked to the local slope gradient and inherited geometries of the previous deposits (Northern and Southern fans). This is particularly the case for middle-fan and down-fan avulsions, which are more easily developed because of limited confinement of the turbidity currents in the distal parts of the basin. However, the

occurrence of very up-fan avulsion before the complete infill of the available space down-fan (accommodation) suggests another external control on sedimentation (Picot et al., 2016). Eustatic control is rejected as the Congo Fan is a perennial system with a permanent connection between the Congo River and the canyon head, which penetrates 30 km inside the estuary, regardless of sea-level variations from 210 ka to the present (Heezen et al., 1964; Van Weering and Van Iperen, 1984; Moguedet, 1988; Droz et al., 1996; Savoye et al., 2000; Babonneau, 2002; Savoye et al., 2009; Picot et al., 2019). The impact of continental uplift since the Pliocene on the morphology of the Congo River watershed, and thus on sediment production and flux, is not well constrained and may even be non-existent, as suggested by the study of Lavier et al. (2001). In contrast, the role of climate on sedimentation in the Congo Fan is well evidenced by multi-proxy studies on the marine reference core KZaï-02 (see Fig. 1 for location and Fig. 2b), which specifically highlight the link between sediment flux and palaeoclimatic signals (Gingele et al., 1998; Molliex et al., 2019; Picot et al., 2019). During the last 210 kyr, the Congo River watershed has been characterised by a succession of humid and arid periods corresponding respectively to interglacial and glacial or highstand and lowstand periods (Schneider et al., 1997; Jahns, 1996; Gingele et al., 1998; Dalibard et al., 2014). The glacial/lowstand episodes (Marine Isotope Stages [MIS] 6, 4, and 2) were characterised by an arid climate synchronous with the development of icecaps at the poles (deMenocal et al., 1993; Leroux, 1993), whereas the interglacial/highstand stages (MIS 7, 5, 3, and 1) were wetter (Schneider et al., 1997; Dupont et al., 2000) and associated with strengthening of the West African monsoon regime (Gingele et al., 1998). In particular, the sediment supply to the ocean has been correlated with 23-kyr precession cycles (Fig. 2), which govern the intensity of the West African monsoon (Schneider et al., 1997; Gingele et al., 1998; Caley et al., 2011). Picot et al. (2019) confirmed that for the last 38 kyr, the primary control of sedimentation has been monsoon-driven climatic changes acting on the liquid and solid fluvial discharges and thus on turbidity current capacity (Fig. 3). The progradation of the system is correlated with humid periods with elevated

transport capacity of turbidity currents. This is because a high-intensity monsoon increases fluvial discharge and chemical erosion, which put fine-grained material into suspension, thus leading to a muddy sediment supply in the turbidite environment. In contrast, retrogradation of depocentres occurred during arid periods. These periods were characterised by low intensity of rainfall, limited runoff, and considerable predominance of mechanical erosion associated with limited vegetation cover on land, thus leading to a decrease in the transport capacity of turbidity currents. Finally, arid/humid transition periods were conducive to major retrogradation and up-fan avulsion followed by new increases of the transport capacity of turbidity currents, which resulted from the onset of precipitation when vegetation cover had not yet colonised the watershed.

3. Data and methods

3.1. DionisosFlow™, a four-dimensional forward stratigraphic model

Based on our objectives, dynamic deterministic modelling was selected as the most appropriate tool because its physical laws of sediment transport lead to the simulation of average sedimentary architecture and facies distribution over time (e.g. Granjeon, 1997). We used the DionisosFlow™ software, which allows simulation of sediment transport and 3D geometric reproduction of sedimentary units from deltaic to deep-sea environments, based on physical processes such as sea-level changes, tectonics, and sediment supply and transport (Granjeon, 1997; Granjeon and Joseph, 1999) (Fig. 4). At each time step, the software quantifies the accommodation (according to basin geometry, subsidence history, and sea-level variation) and sediment supply based on large-scale transport laws (Granjeon, 1997; Granjeon and Joseph, 1999). Two main types of transport mechanisms are defined in the simulation: (i) long-term transport such as water-driven and slope-driven transport and (ii) short-term transport such as debris flows (Granjeon and Joseph, 1999). The transport of particles is governed by a diffusion law, coupled with a continuity equation

for sediment mass conservation, which expresses the sediment flux as a function of slope gradient, water discharge, and diffusion coefficients:

$$Qs,i = vi*(K_{s,i} + K_{w,i} * Qw^m) * \Delta h^n, \quad (1)$$

where Qs,i is the flux of the ith granulometric class (km^2/yr); vi the proportion of the ith sediment class in the sediment flow; $K_{s,i}$ and $K_{w,i}$ are the diffusion coefficients for slope-driven transport (mainly slow creep) and water-driven processes, respectively (km^2/yr), reflecting the transport efficiency in both the marine and continental domains; Qw is the dimensionless local water discharge; Δh is the local gradient of the basin slope; and m and n are constants (usually between 1 and 2) defining a nonlinear equation that reflects the balance between slope- and water-driven transport. Coupling with the mass balance equation allows quantification of the erosion and sedimentation rates of each granulometric class in each cell of the model, and thus the calculation of volumes of deposited sediment. This diffusion process-based software is applicable at a resolution corresponding to a large time scale, from kyr to several Myr, and at the sedimentary basin-scale, from several tens to several hundreds of km². The slope reflects the driving force resulting from the complete conversion of potential energy in kinetic energy (e.g. Paola et al., 1992). Processes that are not associated with water- or slope-driven transport, such as aeolian processes and oceanic currents, are not simulated. Moreover, as the purpose of DionisosFlow™ is to determine the average geometry and facies distribution inside a stratigraphic unit at a given time step, it is likely infeasible to model one-time events (such as floods and storms) and individual flows in the deep-sea environment. Therefore, density-stratified turbidity current flow, as observed in nature, cannot be simulated through the diffusion approach, and some important processes, such as external levee development by flow stripping and overspilling, are not modelled. Consequently, only large-scale and long-term evolution of the turbidite system can be modelled with this method, which fits well with our objective of recreating the successive periods of progradation and retrogradation of sedimentary units identified in the Late Quaternary Congo Fan by Picot et al. (2016, 2019).

A climate module is integrated in the software, providing the possibility to construct curves of *Qs* and *Qw* over time by defining the pattern (such as sinusoidal and sawtooth) and the period of the curve. In addition, the software integrates a module named HEST based on hydrological statistics calculated for five major rivers in the United States (the Eel, Colorado, Mississippi, Hudson, and Delaware rivers). This module allows the simulation of both *Qs* and *Qw* during high- and low-energy events based on their respective durations as well as their relative contributions in terms of sediment supply.

The software CougarFlow™ (OpenFlow Suite) finalises the model calibration by considering the impact of the uncertainties of the input parameters on the simulation results (Fig. 4). This module provides the opportunity to launch a 'multi-realisation simulation' to test the effects of the variations of the input parameters in response surface modelling (RSM, e.g. Gervais et al., 2017; Hawie et al., 2019; Sangster et al., 2019). Then, Monte-Carlo sampling of the RSM can be performed to determine a probabilistic distribution of the responses of the models.

3.2. Strategy and calibration of simulations

In process-based stratigraphic modelling, the stratigraphic organisation of deposits is a function of the temporal evolution of three main parameters—(i) accommodation, (ii) sediment supply from one or several sources at the boundary of the initial grid, and (iii) sediment transport. At the end of the simulation, a large panel of output data is available, such as the thickness of the deposit (and thus its volume), the distribution of sedimentary facies, the evolution of water discharge along the sedimentary system, and the sedimentation rate (Fig. 4).

In our study, the calibration of the model after simulation was mainly based on the architectural parameters defined by Picot et al. (2016) and the deposited sediment volume of each prograding/retrograding cycle inferred from seismic data and computed with the Kingdom Suite software (see Picot et al. (2016) for a complete description of the seismic data used to establish the

architecture of the fan). Isopach maps were constructed after simulations for each architectural cycle, and the sedimentary volumes of compacted sediments were calculated for comparison with the Axial Fan.

The next step was uncertainty analysis of the models using CougarFlow^{TM}. Latin hypercube sampling RSM was used to run 100 simulations of the maximum and minimum values of inputs to predict the responses of the models in terms of sedimentary deposit volumes over time. Then, Monte-Carlo sampling of the RSM was performed to compare the simulated deposit volumes with those calculated for the Axial Fan based on seismic interpretation.

3.3. Model setup

The diffusion process-based approach means that sedimentary processes of transport and deposition are averaged over a given period of time. For all our simulations, the time step was set at 5 kyr to test orbital cycles (with a minimum scale of 23 kyr). The model size extended from Brazzaville in the Congo watershed to the deep-sea environment for a total length of 1,383 km and a width of 468 km (Fig. 5). The cell size was fixed at 6 × 6 km^2, corresponding to the minimum space between two-dimensional (2D) seismic lines. The model boundaries were closed for sediment transport, meaning that all the sediments were deposited inside the defined model size. Closing the model boundaries allowed us to highlight sediment transport inconsistencies regarding the sediment distribution in the real Axial Fan, particularly laterally to the fan axis where the depocentres are well delimited by geophysical cover (Fig. 2).

As mentioned above, during simulation, sedimentary particles were transported and deposited according to three main input parameters (Granjeon et al., 1994):

(i) Accommodation (basin morphology, subsidence, and eustacy): Because of the short simulated time interval, we assumed that accommodation was mainly controlled by flexure and sea-level variation. To define the initial bathymetry of the basin at the starting age of the simulation, we

used the base of the Axial Fan interpreted from seismic data and corrected it based on the flexural deformation linked to the sediment load of the overlying turbiditic deposits according to the calculation methods used by Nygård et al. (2004). The high-resolution LR04 $\delta^{18}O$ curve of Lisiecki and Raymo (2005) and interpreted sea-level variation of Spratt and Lisiecki (2016) were chosen (Fig. 2b) to define eustacy in all simulations. No tectonic subsidence was indicated in the simulations because of the absence of tectonic movement in the margin and deep-sea basin during the last 210 kyr (Lavier et al., 2001).

(ii) Sediment transport (water discharge, lithology, and diffusion coefficient): We assumed that the fluvial discharge in the Congo River ran basinward as gravitational flows according to hyperpycnal transport or slope destabilisation (Heezen et al., 1964; Khripounoff et al., 2003). Mean values of water discharge *Qw* in the Congo River were inferred from the literature (41,000 m^3/s; Laraque et al., 2009, 2013) and then extrapolated from multi-proxy studies, as described in detail in section 3.4. The uncertainties (+/− 4,000 m^3/s) were determined according to the centennial fluctuations measured by Laraque et al. (2013).

Lithologies were limited to sand (grain size of 0.2 mm) and mud (grain size of 0.004 mm), for which compaction laws (by default in the software) were used during simulations. We used a diffusion coefficient for long-term gravity-driven transport of 10^{-2} km^2/kyr for the marine domain and 10^{-3} km^2/kyr for the continental domain, which are reasonable values based on modelling performed on similar sedimentary systems (e.g. Csato et al., 2013; Leroux et al., 2014; Deville et al., 2015). For water-driven transport, we adopted the same values of the diffusion coefficient for long-term and short-term water-driven transport. The calibration of these diffusion coefficients was based on the longitudinal and lateral extents of the simulated deep-sea fan when the *Qw*, *Qs*, and sand/mud ratio were kept constant. Figure 6 shows the high sensitivity of the final geometry of the turbidite system in the deep-sea environment to the diffusion coefficient. Values of 1.5 and 10

km²/kyr, respectively, were chosen for $K_{water,sand}$ and $K_{water,mud}$ for all simulations because they allowed the best reproduction of the general size (length and width) of the Axial Fan deposits.

(iii) Sediment availability*:* The mean value of sediment supply *Qs* was first calculated from the entire volume of the Axial Fan, 7,500 km^3, which yielded a mean *Qs* of 37 km^3/kyr over 210 kyr. The uncertainty related to the resolution of seismic data was +/− 5 km^3/kyr. Then, we defined minimum and maximum values through time of *Qs* based on a BQART approach (Syvitski et al., 2003; Syvitski and Milliman, 2007) performed on the Congo River watershed, which allowed us to fix extreme boundaries for *Qs* in our models as a function of water discharge, basin area, maximum relief, mean temperature, lithology, and trapping efficiency. Using this equation, the sediment flux for the Congo River was quantified for both interglacial and glacial periods. Because of the narrow and steep geometry of the margin, the basin area has remained unchanged over the last 210 kyr. We assumed that the mean maximum relief and lithology also remained constant over the last 210 kyr. We also kept the water discharge constant over time by taking the mean value reported by Laraque et al. (2013). The mean temperature and trapping efficiency in the estuary are sensitive properties related to glacial and interglacial fluctuations. Based on the Community Climate System Models (CCSM – Kutzbach et al., 1998), the mean temperature between latitudes 30°N and 30°S was set at 15 °C during the Last Glacial Maximum and at 20 °C for interglacial periods. Regarding the trapping efficiency, we tested two distinct configurations corresponding to the value assumed by Moguedet (1988), who suggested that between one-third and two-thirds of conveyed sediment may be trapped at the river mouth. Our results show that during the Last Glacial Maximum, the values of sediment supply varied between 24 and 46 km^3/kyr for a high and low trapping efficiency, respectively. Similarly, for the last interglacial period, the sediment supply ranged between 32 and 62 km^3/kyr.

The sand/mud ratio was inferred from core data (sedimentary logs of cores RZCS01, RZCS06, RZCS07, RZCS15, RZCS21, and RZCS25 presented by Picot et al., 2019) and the

morpho-sedimentary map of Babonneau (2002) updated based on our interpretation of seismic volumes of sand (channels) and mud (levees and distal fringes of lobes) facies. This approach indicated relative proportions of sand and mud of 24% and 76%, respectively, during interglacial periods and 30% and 70%, respectively, during glacial intervals for the entire turbidite system. We estimated uncertainties of +/− 4%, linked to the silty parts of cores, which are difficult to attribute to one of these two grain-size classes. Figure 5 summarises all the main input parameters for all of our simulations.

3.4. Simulated scenarios

Based on the assumptions made during the construction of the geological conceptual model (see section 2.3), six main scenarios were tested in the stratigraphic modelling:

Scenario 1 – Autogenic control: As the current dynamics and sinuosity of individual channels were not simulated in our model, only the internal factor of topographic compensation could be addressed in our study. Topographic compensation is here related to the initial bathymetry of the basin (before deposition) and the evolution of the geometry of the sediment deposits themselves through time (e.g. Flood and Piper, 1997; Pirmez et al., 1997). This scenario consists of maintaining all input parameters constant over time during simulations.

Scenario 2 – Sediment fluxes calculated from the seismic volumes of deposits: The relevance of *Qs* calculated from the seismic volumes of deposits for each sedimentary cycle of the Axial Fan (i.e. volumes between depth-converted horizons mapped from a 2D seismic grid) was tested. The seismic volumes were decompacted to determine the mass flux, using the porosity laws of Allen and Allen (2005) for sand and mud. The obtained volumes appeared highly variable over time—1,996 km^3 for cycle A, 1,097 km^3 for cycle B, 3,446 km^3 for cycle C, and 962 km^3 for the youngest and still active cycle D. For a mean sediment density of 1.6 g/cm^3, these values

correspond to *Qs* of 25.9 km^3/kyr between 210 and 130 ka, 16.4 km^3/kyr between 130 and 75 ka, 50.3 km^3/kyr between 75 and 11 ka, and 90.2 km^3/kyr between 11 and 0 ka.

Scenario 3 – Extrapolation of the hydrological regime of the Congo River: The aim was to determine whether turbidity current dynamics are the result of the long-term regime change in the feeding river or short-term 'catastrophic' events related to single high-energy floods. For this purpose, we used the module HEST (see section 3.1).

For the following scenarios 4, 5 and 6, we used marine proxies of water and sediment discharge in reference core data to calculate the evolution of *Qs* and *Qw* through time in our simulations. For this purpose, by indicating the maximum and minimum values of *Qs* and *Qw* presented in section 3.3, we transcribed the curves of marine proxies in values of *Qs* and *Qw* over time. Mean values of *Qs* and *Qw* calculated as described in section 3.3 were then verified based on these calculated curves to verify the viability of the input data over time. It particular, this allowed us to test the impacts of the continental climate and vegetation cover on sediment flux to the deep-sea basin.

Scenario 4 – West African monsoon: Two distinct simulations were considered:

- (4a): *Qs* and *Qw* extrapolated from the West African monsoon curve of Caley et al. (2011) (see Fig. 2b for the curve);
- (4b) and (4c): cycles with a period of 23 kyr for both *Qs* and *Qw* to test the impact of precessional orbital cycles with similar sinusoidal evolution of *Qs* and *Qw* over time (4b) and a 5 kyr phase shift between *Qw* and *Qs* (4c).

Scenario 5 – Marine proxy of vegetation cover changes in the watershed in response to arid and humid conditions: Several studies have demonstrated the reliable use of the pollen

distribution of *Podocarpus* as a proxy for climate/vegetation impact on sediment transfers (Jahns, 1996; Dupont et al., 1998; Jahns et al., 1998; Marret et al., 1999; Dupont et al., 2000; Dupont et al., 2007; Ledru et al., 2007). Dalibard et al. (2014) also suggested that the pollen ratio *Podocarpus*/(*Podocarpus* + rainforest) provides a reliable representation of the nature and latitudinal distribution of vegetation in West Africa. The *Podocarpus*/(*Podocarpus* + rainforest) pollen curve built from the KZaï-02 reference core (Dalibard et al., 2014; see Fig. 2a for location and Fig. 2b for the curve) was used in the simulations. Two assumptions were tested—positive (5a) and negative (5b) correlations between *Qs* and *Qw* through time.

Scenario 6 – Marine proxy of the timing of fluvial discharge in the basin: Gingele et al. (1998) showed that the kaolinite/smectite ratio is a relevant proxy of the timing and intensity of fluvial discharge of the Congo River (see Fig. 2b). We therefore used this ratio measured from the KZaï-02 marine core (Sionneau et al., 2010) to extrapolate both *Qs* and *Qw* over time, by considering positive (6a) and negative (6b) correlations between these two parameters in the same way as in scenario (5).

Finally, for the extrapolation of the evolution of grain size over time, we modulated the sand/mud ratio calculated from seismic and core data using the zirconium/rubidium ratio (Zr/Rb) (measured in the reference core KZaï-02; Fig. 2b), with respect to the average sand and mud proportions calculated for arid and humid periods (see section 3.3). Zr/Rb is known to be a good proxy of grain size distribution and transport efficiency (e.g. Dypvik and Harris, 2001).

4. Results

Approximately 100 simulations were performed based on the six scenarios proposed above. Herein, we focus only on the best-calibrated simulations that present similar overall volumes of deposits in the deep-sea environment to that in the geological model of the Axial Fan (section 2) and suitable general architecture and distribution of depocentres. The primary selection was based on uncertainty analyses performed with CougarFlow^{TM} (section 3.2) to test the viability of the total volume of sediment deposits in the deep-sea environment compared with the Axial Fan. For the selected scenarios, Monte-Carlo risk analysis showed good calibration of the total volume, with P50 varying between 7,284 and 7,353 km^3 (50% of chance that the real response value is equal to or greater than the P50 value), close to the volume of 7,500 km^3 calculated from seismic and bathymetric data for the Axial Fan. The results of these selected simulations were compared with the Axial Fan through two distinct criteria: (i) the general distribution of turbiditic channels illustrated by the simulated sand distribution compared with the traces of channels shown in the bathymetry of the Axial Fan (Figs. 7, 8, and 9) and (ii) the distance to the avulsion point (DA) from a reference point located at the canyon mouth (see section 2.2 for explanation) between the simulations (in orange) and the Axial Fan (in blue, from Picot et al., 2016) (Fig. 10). DA is the best architectural parameter to highlight the dynamics of prograding and retrograding cycles of the turbidite system over time. When such cycles were identified, we calculated the simulated volume of each cycle and compared it with the volume obtained from the seismic interpretation of the Axial Fan (see section 3.4). It is important to note that none of the simulations succeeded in reproducing the positions of the currently active channels of cycle D located on a high relief area in the northern part of the fan (Figs. 7, 8, and 9). The positions of these channels therefore were not used as criteria for the primary selection of the best simulations; their absence in our simulations is discussed below.

The results of channel distributions of the different simulated scenarios (see section 3.4) are presented in Figure 7 for scenario 1 (autogenic control), scenario 2 (sediment fluxes calculated from seismic volumes), and scenario 3 (extrapolation of the hydrological regime of the Congo River); in

Figure 8 for the simulations of the West African monsoon in scenario 4a (model of Caley et al., 2011), scenario 4b (sinusoidal curves with a 23-kyr period), and scenario 4c (sinusoidal curves for *Qw* and sawtooth pattern for *Qw* with a 23-kyr period); and in Figure 9 for simulations based on proxies of the KZaï-02 reference core with the different scenarios 5 (marine proxy of vegetation cover changes in the watershed in response to arid and humid conditions) and 6 (marine proxy of the timing of fluvial discharge in the basin). The preliminary comparison of channels and avulsion distribution permitted us to exclude some scenarios. This was the case for scenarios 1, 2, and 3 (Fig. 7a, 7b, and 7c), as all avulsions occurred in a position that was too distal from the reference point, 300 to 400 km compared with the main avulsion points in the Axial Fan at 200 km (Fig. 2). In these scenarios, we noted the absence of architectural cycles and the lack of middle-fan depocentres. In scenarios 4b (Fig. 8b) and 6b (Fig. 9d), the simulated sediments were shifted too far to the south compared with the real data, even going beyond the limit of the model.

Among the remaining simulations with general architecture very similar to the general outline of the Axial Fan, the examination of simulated progradational/retrogradational cycles (with the distance to avulsion points DA) constituted the last discriminant parameter to choose the best-fit scenarios (Fig. 10). As noted earlier, DA highlights progradational/retrogradational cycles with volumes of deposits that can be compared with volumes calculated based on seismic data for the Axial Fan. Then, Monte-Carlo risk analysis was performed using CougarFlow^{TM} for each simulated architectural cycle to define the uncertainties of the results (see section 3.2). For scenarios 4a (Fig. 10a) and 6a (Fig. 10e), only three progradational/retrogradational cycles were simulated, whereas four cycles were observed in the Axial Fan. Scenario 5a was also rejected, even though the timing of the main avulsion points was consistent with that of the Axial Fan. However, the distances to the avulsion point defining the last cycle D and the end of cycle C did not fit with the geological reality (Fig. 10c).

Consequently, two scenarios were able to reproduce the Axial Fan architectural evolution, regarding the timing and position of up-fan avulsions and the simulated volumes of progradational/retrogradational sedimentary cycles: (i) scenario 4c, corresponding to precession cycles with a sawtooth pattern of *Qs* and sinusoidal evolution of *Qw* (Fig. 10b), and (ii) scenario 5b, simulating arid/humid conditions inferred from the *Podocarpus*/(*Podocarpus* + rainforest) pollen ratio with a negative correlation between *Qs* and *Qw* over time (Fig. 10d). For the sake of simplicity, we refer to these best-fit models hereafter as the precession simulation for scenario 4c and the vegetation simulation for scenario 5b.

It should be pointed out that even with these best-fit simulations, some differences exist with respect to the architectural parameters calculated by Picot et al. (2016) for the Axial Fan. The first is an additional volume of around 500 km^3 for the first cycle A, between 210 and 130 ka. This difference may be explained by the fact that the total longitudinal extent of this cycle is unknown (bathymetric and seismic data are lacking in the most distal part of the basin). Another difference arises for cycle C, for which simulations show a well-developed symmetrical progradational/retrogradational cycle not observed by Picot et al. (2019). This difference may be related to the lack of architectural data for the early part of cycle C because of the existence of a cluster of stacked channels and lobes ('undifferentiated unit package 2' of Picot et al., 2019) for which it was not possible to measure avulsion lengths. Lastly, for both simulations, we observed a time shift of cycles B and A covering the period between 70 and 200 ka, for which the time constraints are poor and possibly not accurate (Picot et al., 2019). Indeed, to achieve a perfect match of the timing of these cycles, it appears to be necessary to shift the simulation curves approximately 10 kyr older during this period.

5. Interpretation and discussion

5.1. Best-fit simulations versus geological model over the last 38 kyr

Several studies have claimed that the timing and positions of channel avulsions, which govern the architectural evolution of deep-marine fans, are linked to the interconnection over time between both internal (such as topographic compensation, current dynamics, and channel sinuosity) and external controls (such as tectonics and climate) (Kolla, 2007; Stouthamer and Berendsen, 2007). Deciphering the respective importance of distinct forcings is challenging, and our 3D stratigraphic modelling is a useful tool in the attempt to individualise the relative effects of these controls. Our results showed the following.

(1) Topographic compensation (the only internal control tested by our model) played a minor role in the development of progradational/retrogradational cycles at the resolution scale of the simulation, as shown by the poor calibration of the simulation testing autogenic control (scenario 1; Fig. 7a), and more specifically in the development of up-fan avulsions (Fig. 11). Levee instabilities and breaching (e.g. Ortiz-Karpf et al., 2015), which are not simulated in DionisosFlow^{TM}, are rarely observed in the Late Quaternary Congo Fan (Babonneau, 2002; Picot et al., 2016), which suggests that such processes can be neglected here. This finding highlights the dominant role of external controls on prograding/retrograding cycles.

(2) Catastrophic events do not simulate the most proximal up-fan avulsions. Scenario 2 aimed to test the calculation of sediment discharge based on the volume of sedimentary deposits within each prograding/retrograding cycle defined by Picot et al. (2016, 2019). Such a simulation necessarily implies a step-like evolution of sediment discharge and consequently rapid variations through time. This explains why only one channel was active throughout the simulation (Fig. 7b), as it was re-used with each sudden increase of sediment supply. The same explanation can be proposed for the simulation that used the module of catastrophic high-energy events (scenario 3; Fig. 7c). It appears that a more progressive evolution of sediment and water discharge is necessary to produce separated channel systems and thus individual progradational/retrogradational cycles.

(3) Consequently, we can first confirm through stratigraphic modelling that the impact of climate changes on *Qs* and *Qw* is a dominant influence on the architectural evolution of the deep-sea fan, as shown by the two best-fit simulations based on the precession cycle controlling the West African monsoon (Caley et al., 2011) and the change of vegetation cover based on the pollen proxy in marine cores.

Fan activity during the last 38 kyr corresponds to the best-constrained chronostratigraphic interval based on the work of Picot et al. (2019), and allows the viability of our simulations to be assessed (Fig. 12). Both of the best simulations, the precession and vegetation scenarios (scenarios 4c and 5b respectively), show very well-suited evolution of progradation and retrogradation during this period, with nearly perfect superposition of the curves showing the distance of avulsion points over time (Fig. 10b and 10d). The slight time shift of curves was likely only caused by the large time step of 5 kyr. Between 38 ka and 28 ka, a general progradation of the system was indicated (Fig. 13a-t1), with sediments transported to the down-fan area more than 700 km away from the canyon mouth. Cross-sections in the simulations reveal prograding clinoforms that exhibit similarities with geometries observed in longitudinal seismic profiles of the Axial Fan (Fig. 13b). The down-fan area is mainly characterised by muddy deposits with approximately 85% mud, which is quite consistent with the piston core observations indicating 82% +/− 4% mud in the terminal lobes. This period of progradation corresponds to the end of MIS 3, which was a humid climate stage (Schneider et al., 1997; Dupont et al., 2000) (Fig. 12), consistent with the geological model of Picot et al. (2019). In our simulations, the *Qw* of the Congo River increased and the *Qs* was low. These conditions correspond to an important transport capacity explaining the maximal progradation of the sediments (Mutti and Normark, 1987; Reading and Richards, 1994; Galloway, 1998). At the climatic transition between humid (MIS 3) and arid (MIS 2) periods, an aggradation of depocentres occurred just before large-scale retrogradation (Fig. 12 and 13a-t2), possibly related to a backfilling effect of channelised structures (Fig. 11), as also indicated by Hodgson et al. (2006)

based on their ‘tripartite model’ in the Karoo Basin. Such a process would progressively lead to the retrogradation of depocentres, characterised by several middle-fan avulsions. Middle-fan avulsions would create well-individualised laterally migrating depocentres, which are comparable with those observed in the seismic data (Fig. 13c). The retrogradation of the system started when *Qs* and the sand fraction were at their maxima; that is, when the Congo River exhibited its minimum transport capacity. The retrogradation progressively continued as *Qw* and *Qs* decreased until the arid/humid climatic transition at 15 ka. This transition was marked by a proximal up-fan avulsion located less than 200 km from the submarine canyon mouth, showing overall northward stacking of sand-rich deposits over time (Fig. 13d). Up-fan avulsion was directly followed by an abrupt progradation of depocentres marking the onset of the currently active cycle D (Fig. 13a-t3 and 13d). Up-fan avulsion and progradation during the humid period was a consequence of the significant increase in river transport capacity while the sediment charge conveyed was still low and *Qw* was increasing (Fig. 13a-t3).

However, a significant difference from the geological model of the Axial Fan was associated with the position of the currently active turbidite channel in the northern part of the system, abnormally perched on the previous Northern Fan (Fig. 2a and 14). None of our simulations successfully simulated the correct position of this channel. The best-fit simulations showed an active channel in the northern part, but it was limited northward by the elevation of the Northern Fan (Fig. 14). The position on a topographic high and the overdeepening of the current active channel of the Axial Fan are attributed to very muddy flow over a long period of time, which concentrated turbulence at the base of the channel through the construction of high external levees (Babonneau et al., 2010). In this configuration, greater development of external levees by flow stripping and overspill of the muddy material is associated with greater turbulence, and therefore increased channel deepening. Our model does not simulate these local turbulences, which explains why the simulated turbidity currents did not migrate on the high points of the Northern Fan.

553 Despite the position of the currently active turbidite channel, the simulated progradation and
554 retrogradation phases during the last 38 kyr are consistent with the geological model of Picot et al.
555 (2019). The stratigraphic modelling thus confirms that the variation of liquid and solid discharge in
556 response to climate/vegetation coupling in the watershed was the main forcing factor of the
557 progradational/retrogradational cycles.
558
559 **5.2. Extrapolation to 210 kyr**
560 The precession and vegetation simulations have thus been validated by the well-calibrated
561 chronostratigraphic model of Picot et al. (2019) between 0 and 38 ka. We now aim to extrapolate
562 these models on a longer time scale over the last 210 kyr.
563 For both the precession and vegetation simulations, the results show the succession of four
564 main progradational/retrogradational cycles, respectively between 210 and 130 ka, 130 and 85 ka,
565 85 and 15 ka, and 15 and 0 ka (Fig. 10B, 10d and 14). Each cycle is characterised by the same
566 geometric evolution, which can be sequentially divided into the three steps as described in section
567 5.1: (i) up-fan avulsion followed by (ii) maximum progradation of depocentres, and (iii) progressive
568 retrogradation of the system (Fig. 13a). The curves of the distance to avulsion points from
569 geological data and from simulations can be superimposed with a time shift of approximately 10
570 kyr (Fig. 10b and 10d), which confirms that the architectural evolution of the fan over the last 210
571 kyr was accurately reproduced. The time shift may be explained by the time step of the simulations,
572 and also by the uncertainties of ages obtained from dating based in geological data, as these dates
573 are not yet sufficiently accurate at this time scale. The conceptual architectural model defined in
574 section 2 for the last 38 kyr thus seems to be applicable to the entire activity period of the Axial Fan.
575 Over the last 210 kyr, sedimentation has been controlled by the concomitant variation of
576 sediment and water discharge in response to climate changes. Retrogradation of the turbidite system
577 has always been initiated when the sediment discharge was high and the river runoff decreased

during arid periods (Fig. 12). Following these retrogradational periods, proximal up-fan avulsions and maximum depocentre progradation were induced by maximum water discharges and minimum conveyed sediment loads at the arid/humid climate transition. However, the mechanism of middle-fan avulsions is different from that involved in large-scale up-fan avulsions. Our simulations show that up-fan avulsions are linked to high-magnitude variations of the volume of sediment transported from the continent to the sedimentary basin. In contrast, the development of middle-fan and down-fan avulsions was more sensitive to the evolution of the sand fraction in the sediment supply, as these events were always synchronous with abrupt increase of the sand fraction and thus directly linked to the decrease in flow transport efficiency (Mutti and Normark, 1987; Reading and Richards, 1994; Galloway, 1998). We assume that this abrupt increase of sandy material (Fig. 12) may be linked to the destabilisation and transfer of river mouth sand bars observed in the present at the head of the canyon during high river runoff and canyon flushing events (Moguedet, 1988).

5.3. Source-to-sink interpretation: climate/vegetation coupling

We have confirmed that climate/vegetation coupling controlled the architecture of the fan throughout its entire period of sedimentation. Interpretation of the input data of our simulations allowed identification of the geological forcing parameters involved in the architectural evolution of the fan.

Implications of the precession simulation

Among all the simulations controlled by precession, we herein highlight the need to simulate a sawtooth pattern of *Qs* with an abrupt rise, often synchronous with an increase in the sand fraction, followed by a gradual drop (Fig. 12). Abrupt increase in *Qs* induces major retrogradation of the turbidite system as the transport capacity decreases. The maximum *Qs*, coeval with a high *Qw* and high sand fraction, likely indicates the direct transfer of sediment from the

603 continent to the deep-sea basin during river flooding that caused the destabilisation of sandy river
604 mouth bars (Moguedet, 1988). Unlike some models for turbidite systems, such as the Makran
605 system (Bourget et al., 2011), even though arid climate conditions in the Congo River watershed
606 induced enhanced mechanical erosion in comparison with chemical weathering, such conditions do
607 not imply the development of large sandy turbidites. Rather, an arid climate in the Congo watershed
608 is more favourable to temporary trapping of coarse-grained sediments during aggradation of river
609 channel beds (e.g. Blum and Straffin, 2001), floodplain storage (Molliex et al., 2019), and the
610 formation of river mouth bars at the entry of the submarine canyon (Moguedet, 1988). The trapping
611 of coarse-grained materials persisted until river runoff was sufficient to convey such a load, marked
612 by a maximum *Qw* in the simulation. In contrast with the hypothesis of Picot et al. (2019), which
613 related proximal up-fan avulsions to an increase in sediment load, the simulated proximal up-fan
614 avulsions corresponded to an increase in the river runoff *Qw* and a drop of the conveyed sediment
615 load *Qs* (Fig. 12). In the precession simulation, the up-fan avulsion and the following major
616 progradation of the system were only caused by the increase of turbidity current transport capacity
617 when the monsoon intensity was high and chemical weathering was predominant on land, implying
618 a large mud supply in the turbidite environment.
619
620 ***Implications of the vegetation simulation***
621 The vegetation simulation showed similar architectural evolution to that of the precession
622 simulation, despite differences in inputs. The evolution of *Qw* in both simulations was very similar,
623 whereas the evolution of *Qs* differed. The *Qw* is probably more important than *Qs* in the timing of
624 progradational/retrogradational cycles because when the sediment load is high, considerable water
625 discharge is needed to efficiently transport sediments from the continent to the deep-sea
626 environment. Consequently, the difference in *Qs* evolution between the two simulations represents a
627 difference in the geological process of sediment production and trapping on land. In the vegetation

simulation, the maximum sediment production occurred during arid periods, and sediments were trapped until the maximum water discharge was reached. The curve of continental vegetation changes in our simulation was used as a proxy of the modifications of vegetation cover in the Congo watershed in response to successive humid/arid climate oscillations, themselves governed by the West African monsoon (Hoelvoeth et al., 2001; Weldeab et al., 2007; Dupont, 2011; Dalibard et al., 2014). That is why the use of this curve yielded the same results as the precession simulation that simulates the variations of monsoon intensity. Expansion of vegetation cover is expected to decrease the magnitude of river runoff and the sediment yield, according to the balance between mechanical and chemical erosion, because of the reduction of rainfall impact, modification of soil moisture, increased infiltration, increased evapotranspiration, root mechanical reinforcement, and increased surface stability favoured by the weight of vegetation (e.g. Renard et al., 1997). This concept implies a negative correlation over time between vegetation cover and soil erosion and runoff (e.g. Gaillardet et al., 1999; Zhou et al., 2008; Hou et al., 2016), and thus a negative correlation between water and sediment discharge over time, as demonstrated in the Nile River (Krom et al., 2002; Ducassou et al., 2009), the Niger Delta (Zabel et al., 2001), and the Bengal Fan (Weber et al., 2003). Our vegetation simulation results are consistent with these observations, with the best simulation obtained through a negative correlation between *Qs* and *Qw* over time (Fig. 12).

5.4. Insights and limits of diffusion process-based stratigraphic modelling

Since the 1990s, 3D forward modelling has been used to test hypotheses in geological conceptual models through an ‘inversion loop’ that helps to extrapolate field and geophysical data when the resolution is temporally or spatially limited. However, very few process-based modelling studies have attempted to reproduce the architectural evolution of turbidite systems along the deep-marine domain at the basin-scale (e.g. Groenenberg et al., 2009; Groenenberg et al., 2010; Gvirtzman et al., 2014; Deville et al., 2015; Hawie et al., 2018).

This study shows that a nonlinear water-driven diffusion equation allows the reproduction of basinward/landward migration of depocentres over time with channelised systems whose geometry is comparable to channel–levee–lobe systems observed in geophysical data (Figs. 13 and 14). The resolution scale of stratigraphic modelling is similar to the horizontal resolution of geophysical data, which permits comparison with architectural parameters measured in the simulations and those measured directly through geophysical interpretation. In addition, the numerical approach allows interpolation between seismic lines (in our case, spacing of 2D seismic acquisition can reach 26 km, four times the resolution of the stratigraphic grid in our model) and provides simulated total volumes of sediments deposited in the area, including the extrapolation of zones not fully covered by geophysical and core data (both laterally and vertically). Furthermore, the simulation provides better 3D distribution of the lithological facies (sand/mud ratio), especially at depths that cannot be reached by piston cores (which usually reach maximum depths of 20–30 m), and thus reveals crucial information to understand reservoir quality. Most importantly, this numerical modelling provides quantification of the sediment flux over time and permits independent investigation of the relative impacts of *Qs*, *Qw*, and the sand fraction in the Congo turbidite depocentres defined based on various internal and external factors. Our simulations demonstrate the relevance of using climate and environmental proxy curves (such as pollen, $\delta^{18}O$, and kaolinite/smectite) to simulate the sediment supply from source to sink in this type of stratigraphic modelling.

However, some caution must be taken when the processes at the origin of the depositional stacking pattern are interpreted, as diffusion process-based modelling averages the mechanisms of sediment transport and deposition at a given time step. Therefore, we must assume that all geological processes acting in the turbidite system dynamics can be averaged within a 5 kyr period in our study. This assumption is not true at the scale of individual channels with activity that extends from 1 to several kyr, according to Picot et al. (2019). Other external forcings are also ignored because of this time scale, such as semi-precession cycles with periods of 5.5 to 11.5 kyr

(Berger and Loutre, 1997) or Heinrich cycles with periods of 6 to 8 kyr (Weldeab et al., 2007), which have been suspected by Dalibard et al. (2014) and Picot et al. (2016) to play a role in the development of sedimentary sub-cycles in the Late Quaternary Congo Fan. However, because our objective was to analyse the controlling parameters responsible for the development of long progradational/retrogradational sedimentary cycles, the use of diffusion process-based modelling is relevant here.

Our forward stratigraphic model extrapolates the geological processes on land from marine data, which necessarily implies uncertainties in the interpretations. First, the response time between the climate, geological processes, and sediment yield on land is not well known, especially for large watersheds such as the Congo sedimentary system (Gasse, 2000). Second, it is challenging to evaluate the timing of sediment transfers toward deep-marine basins. Ducassou et al. (2009) reported an instantaneous response of the river and submarine fan to millennial-scale changes in climate in the Nile drainage system, with a time scale compatible with the time resolution of our model. In the case of the Congo Fan, the turbidite system is permanently connected to the feeding river through the submarine canyon; therefore, we assume that the behaviour of the submarine sedimentary system also reflects the geological processes in the watershed. Molliex et al. (2019) modelled the hydro-sedimentary evolution for the Congo River watershed over the last 155 kyr using the HydroTrend model (Syvitski et al., 1998; Kettner and Syvitski, 2008). Incorporating the evolution of the HydroTrend model sediment discharge in DionisosFlow^{TM} failed to reproduce the geological model. Instead, the simulation showed the activity of only one channel that avulsed exclusively in the most distal part of the deep-marine basin. The main reason for this inconsistency was that only the suspended sediment load was simulated by Molliex et al. (2019), even though coarse-grained material represents up to 30% of the sediment budget in the Late Quaternary Congo Fan and is probably transported as bedload. An abrupt supply of sandy sediments induces a decrease in turbidity current transport capacity and thus can be responsible for avulsion and

retrogradation of the fan and is of primary importance in the architectural evolution of the fan. Catastrophic destabilisations of sandy river mouth bars at the head of the submarine canyon may play a key role in the architectural evolution of the deep-sea fan, but the sedimentary processes in the estuarine zone of the Congo River are not well known. In addition, a large portion of the eroded matter of the Congo watershed is transported as dissolved load. This silica-rich dissolved load may quickly precipitate via biogenic processes when it reaches the marine environment, thus strongly increasing the sediment supply through the formation of siliceous biogenic sediment (comprising between 5% and 30% of Congo-fan deposits; Schneider et al., 1997; Hatin et al., 2017), or via rapid degradation into authigenic K- and Fe-rich aluminosilicates (Michalopoulos and Aller, 2004), which are also present in the Congo Fan deposits (Giresse et al., 1998). In addition, coastal currents and tidal effects have not yet been implemented in DionisosFlow™, although the impacts of such currents on sediment transport are assumed to be weak compared with the hyperpycnal flows in the case of the Congo River. Consequently, our work demonstrates that the extrapolation of marine proxies of climatic and environmental changes in the watershed is an efficient tool to recreate the 3D architecture of turbidite systems, although progress must be made in linking stratigraphic modelling with onshore hydrogeological simulations to construct a complete source-to-sink geological model.

6. Conclusions

This study presents for the first time the use of the diffusion process-based stratigraphic forward model DionisosFlow™ to constrain the progradation/retrogradation cycles of a submarine fan at the basin-scale, by examining the case of the Late Quaternary Congo Fan. Simulation viability was tested based on the geological model proposed by Picot et al. (2019), which emphasises the role of climate changes and the impact of induced geological processes on the architectural evolution of the fan during the last 38 kyr. Our main objective was first to confirm this

model through numerical modelling and then to attempt to extrapolate it throughout the entire activity period of the fan over the last 210 kyr, a period not well constrained by dating methods. This diffusion process-based model was found to be a reliable and efficient tool for the simulation of sedimentary progradation/retrogradation cycles as a function of marine and continental proxies. Several key points must be retained from this work:

- Simulations modelled the correct organisation of the channel–lobe system in the deep-sea environment using a nonlinear diffusion equation for sediment transport.
- The horizontal and vertical resolutions of this model were high enough to verify the viability of simulations through comparison with geophysical and marine core data. Once validated, the simulations also allowed us to image sediment deposits where geophysical data were lacking, such as between seismic lines and marine cores.
- The water-driven diffusion process-based model permitted us to study the relative impacts of the variations of sea-level, tectonics, sediment and water discharges, and the sand fraction on the behaviour of the turbidite system. Forward stratigraphic modelling provided the opportunity to test an infinite number of scenarios, particularly with input data defined from marine and continental proxies of climate changes. Consequently, the architectural evolution of the submarine fan could be linked to geological changes in the watershed through a source-to-sink approach. Our best-fit scenarios confirmed that climate/vegetation coupling was the main forcing factor in the architectural evolution of the Late Quaternary Congo Fan over the last 210 kyr.
- The interpretation of hydrogeological processes on the continent established here for the Late Quaternary Congo sedimentary system cannot be generalised for all turbidite systems, as the perennial connection between the Congo River and the submarine canyon induced a direct response between sedimentary processes on land and sediment transfer to the deep-sea fan.
- Source-to-sink analysis by incorporating output data of HydroTrend hydrological modelling of the Congo River watershed (Molliex et al., 2019) was not found to be viable, primarily because

753 only the suspended load fraction was modelled at the outlet of the watershed, not the bedload.
754 Therefore, efforts are still required to improve the integration of continental hydro-sedimentary
755 modelling with stratigraphic modelling in the deep-sea environment.

756 Knowledge of the stratigraphic evolution of deep-marine sedimentary systems helps us to
757 understand the architecture of economic reservoirs (for energy, storage, etc.) as well as potential
758 terrestrial pollutants, as turbidite systems are considered major sinks for wastes conveyed by rivers,
759 particularly microplastics (Kane et al., 2019).

Figure captions

Figure 1: a. Map of the Congo sedimentary system from the Congo River watershed to the Late Quaternary submarine fan (modified from Picot et al., 2019). b. Three-dimensional view of the Congo sedimentary system reconstructed from the compilation of bathymetric data from the Guiness (Cochonat and Robin, 1992; Cochonat, 1993), Zaïango (Cochonat, 1998; Savoye, 1998), and Reprezaï (Marsset and Droz, 2010; Droz and Marsset, 2011) oceanographic cruises and ETOPO1 (Amante and Eakins, 2008) in the watershed (vertical exaggeration x30). Red boxes indicate the sediment budget from the Congo River to the submarine fan. Black boxes illustrate the forcing factors potentially controlling the sediment supply in the watershed and deposition in the deep-sea environment. The location of the reference marine core KZaï-02 is indicated.

Figure 2: Geological interpretation of the Axial Congo Fan (210 kyr to present) from Picot et al. (2016, 2019). a. Channel–lobe map with the location of the reference core KZaï-02 (red star). b. Multi-proxy study. From left to right: architectural diagrams of the fan (channel length in dark blue, distance of avulsion points in light blue—see the sketch below for explanation), $\delta^{18}O$ curve of Lisiecki and Raymo (2005), proxies from the reference core KZaï-02, *i.e.*, the *Podocarpus*/(*Podocarpus* + rainforest) pollen ratio (Dalibard et al., 2014), kaolinite/smectite ratio (Sionneau et al., 2010), zirconium/rubidium (Zr/Rb) ratio (Picot et al., 2019), and West African monsoon curve (Caley et al., 2011). The grey areas correspond to the timing of increased sediment flux in the marine environment inferred from the variations of the kaolinite/smectite ratio (Sionneau et al., 2010).

Figure 3: Geological conceptual model proposed by Picot et al. (2019) emphasising the role of humid/arid climate fluctuations in the architectural evolution of the Congo Axial Fan during the last 38 kyr. See the text for explanation.

Figure 4: Inversion loop illustrating the simulation strategy of 3D forward stratigraphic modelling performed with DionisosFlow™ supplemented by uncertainty analysis conducted with CougarFlow™. The confrontation between the geological conceptual model and modelling results is crucial to obtain a relevant source-to-sink model of the architectural evolution of the study area and to test the roles of the different forcing factors of sedimentation.

Figure 5: Model setup for the 3D forward stratigraphic modelling. Top: initial bathymetry at 210 ka in the simulation (base surface of the Axial Fan) and position of the sediment source. Below: synthesis of the different input parameters described in the text.

Figure 6: Simulated sand thickness in the fan as a function of the water-driven diffusion coefficients for sand ($K_{water,sand}$) and mud ($K_{water,mud}$). The intermediate configuration was chosen for our simulations ($K_{water,sand}$ = 1.5 km^2/kyr; $K_{water,mud}$ = 10 km^2/kyr).

Figure 7: Distribution of simulated sand thickness in the deep-sea environment at the end of simulation for scenarios 1 (autogenic control), 2 (*Qs* calculated from the volume of deposited sediment deduced from seismic data), and 3 (extrapolation of the hydrological regime of the Congo River). Axial Fan channels from Picot et al. (2016) are reported on the maps (orange line: currently active channel; black lines: preceding channels). The point R is the reference point used by Picot et al. (2016) and in this study to measure the distance to avulsion points.

Figure 8: Maps illustrating the distribution of sand thickness in the deep-sea environment at the end of simulation of scenario 4, the West African monsoon: (4a) monsoon model of Caley et al. (2011); (4b) precession: 23 kyr cycle with concordant sinusoidal curves for *Qs* and *Qw*; (4c) precession: 23 kyr cycle with sinusoidal curves for *Qw* and a sawtooth pattern of *Qs* with a time shift of 5 kyr between the two curves. Axial Fan channels from Picot et al. (2016) are reported on the maps (orange line: currently active channel; black lines: previous channels). The point R corresponds to the reference point explained in Fig. 7.

Figure 9: Maps illustrating the distribution of sand thickness in the deep-sea environment at the end of simulations for the scenarios of: the impact of vegetation cover based on the pollen ratio of *Podocarpus*/(*Podocarpus*/rainforest) in the KZaï-02 marine core with scenario 5a (positive correlation of *Qs* and *Qw* over time) and scenario 5b (negative correlation of *Qs* and *Qw* over time); the timing of fluvial discharge based on the kaolinite/smectite ratio in the KZaï-02 marine core with positive (scenario 6a) and negative (scenario 6b) correlations of *Qs* and *Qw* over time. Axial Fan channels from Picot et al. (2016) are reported on the maps (orange line: currently active channel; black lines: previous channels). The point R corresponds to the reference point explained in Fig. 7.

Figure 10: Left: Architectural diagrams of best-fit simulations illustrating the evolution of distances (km) to avulsion points (light blue) compared with the same parameter calculated from the geological model of the Axial Fan (green) (Picot et al., 2019). Right: Volume (km^3) of progradational/retrogradational cycles (dark blue: simulated volumes in DionisosFlow™; brown: volumes in the Axial Fan calculated from seismic interpretation).

Figure 11: Three-dimensional view of the turbidity flow pathway (in red) during the main avulsion: a. t1 – Initial configuration before avulsion. b. t2′– Middle-fan avulsion simulated in scenario 1,

833 autogenic control, which essentially considered the role of topographic compensation. c. Up-fan
834 avulsion simulated in the vegetation simulation.
835
836 **Figure 12:** Evolution over time of the input parameters *Qs* and *Qw* for the vegetation simulation
837 (red bold lines) and the precession simulation (purple dashed lines), and the sand fraction in green,
838 which was similar in both simulations. The timing of simulated up-fan (bold black lines) and
839 middle-fan (dashed black lines) avulsions is also indicated, as well as progradational and
840 retrogradational phases in the right part of the graph (black arrows). MIS: Marine Isotope Stage;
841 grey and white horizontal bands: arid and humid periods, respectively.
842
843 **Figure 13:** Architectural evolution of a sedimentary cycle obtained in both best-fit simulations
844 (vegetation and precession simulations). a. Successive stages of an architectural cycle illustrated
845 from the distribution of channel deposits (in red), lobe deposits (sandy in yellow and muddy in
846 orange), and overflow muddy deposits (in black): (t1) maximum progradation, (t2) aggradation and
847 retrogradation, and (t3) up-fan avulsion. E–W-oriented white arrows: progradation or retrogradation
848 directions; N–S-oriented white arrows: lateral migration of depocentres. The circles indicate the
849 relative proportions of sand and mud calculated in the simulation. b. and c. Comparison between
850 cross-sections of the sand fraction in the simulations and seismic profiles in the Late Quaternary
851 Congo Fan for (b) the progradational phase (AA′, location at a-t1) and (c) the retrogradational phase
852 associated with middle-fan avulsions (BB′, location at a-t2). d. Block diagrams showing the water
853 discharge value (m^3/s) (illustrating the turbidity flow pathway) in the simulation during the up-fan
854 avulsion events. CC′ is a cross-section of the sand fraction in the proximal avulsion node (location
855 at a-t3).
856

Figure 14: Transverse cross-section of the middle-fan zone across the final geometry of the vegetation simulation (see Fig. 9b for location). This section illustrates the overall northward migration of architectural cycles (A, B, C, and D) over time, as well as the incorrect positions of the simulated active cycles, which are not positioned on the topographic high formed by the Northern Fan as is the case in the real fan.

Bibliography

Allen, P., Allen, J., 2005, Basin analysis, Principles and Applications, 549 pp., Blackwell Publishing Ltd, Second Edition.

Alsdorf, D., Beighley, E., Laraque, A., Lee, H., Tshimanga, R., O'Loughlin, F., Mahé, G., Dinga, B., Moukandi, G., Spencer, R.G.M., 2016. Opportunities for hydrologic research in the Congo Basin. Rev. Geophys. 54, 378–409.

Alzaga-Ruiz, H., Granjeon, D., Lopez, M., Seranne, M., Roure, F., 2009. Gravitational collapse and Neogene sediment transfer across the western margin of the Gulf of Mexico: Insights from numerical models. Tectonophysics 470, 21–41.

Amante, C., Eakins, B. W., 2008. ETOPO1 1 Arc-Minute Global Relief Model: Procedures, Data Sources and Analysis, National Geophysical Data Center, NESDIS, NOAA, US Dept. Commerce, Boulder, CO, USA.

Anka, Z., Séranne, M., Lopez, M., Scheck-Wenderoth, M., Savoye, B., 2009. The long-term evolution of the Congo deepsea fan: A basin-wide view of the interaction between a giant submarine fan and a mature passive margin (ZaiAngoproject). Tectonophysics 470, 42–56.

Anka, Z., Séranne, M., 2004. Reconnaissance study of the ancient Zaire (Congo) deep-sea fan.(ZaiAngo Project). Mar. Geol. 209, 223–244.

Armitage, D.A., McHargue, T., Fildani, A., Graham, S.A., 2012. Postavulsion channel evolution: Niger Delta continental slope. Am. Assoc. Pet. Geol. Bull. 96, 823–843.

Babonneau, N., Savoye, B., Cremer, M., Bez, M. (2010). Sedimentary architecture in meanders of a submarine channel: detailed study of the present Congo turbidite channel (Zaiango project). Journal of Sedimentary Research, 80(10), 852-866.

Babonneau, N., 2002. Mode de fonctionnement d'un chenal turbiditique méandriforme: Cas du Système Turbiditique actuel du Zaïre. PhD thesis, Univ. Bordeaux I, Bordeaux. Université Bordeaux 1.

Berger, A., Loutre, M.F., 1997. Intertropical latitudes and precessional and half-precessional cycles. Science (80-.). 278, 1476–1478.

Blum, M.D., Straffin, E.C., 2001. Fluvial responses to external forcing: examples from the French Massif Central, the Texas Coastal Plain (USA), the Sahara of Tunisia, and the lower Mississippi Valley (USA). River Basin Sediment Syst. Arch. Environ. Chang. Balkema, Rotterdam 195–228.

Bourget, J., Zaragosi, S., Ellouz-Zimmermann, N., Mouchot, N., Garlan, T., Schneider, J., Lanfumey, V., Lallemant, S., 2011. Turbidite system architecture and sedimentary processes along topographically complex slopes: the Makran convergent margin. Sedimentology 58, 376–406.

Broucke, O., Temple, F., Rouby, D., Robin, C., Calassou, S., Nalpas, T., Guillocheau, F., 2004. The role of deformation processes on the geometry of mud-dominated turbiditic systems, Oligocene and Lower Middle Miocene of the Lower Congo basin (West African Margin). Mar. Pet. Geol. 21, 327–348.

Brovkin, V., Claussen, M., Petoukhov, V., & Ganopolski, A. (1998). On the stability of the atmosphere-vegetation system in the Sahara/Sahel region. Journal of Geophysical Research: Atmospheres, 103(D24), 31613-31624.

Burgess, P. M., Masiero, I., Toby, S. C., Duller, R. A., 2019. A big fan of signals? Exploring autogenic and allogenic process and product in a numerical stratigraphic forward model of submarine-fan development. Journal of Sedimentary Research, 89(1), 1-12.

Caley, T., Malaizé, B., Revel, M., Ducassou, E., Wainer, K., Ibrahim, M., Shoeaib, D., Migeon, S., Marieu, V., 2011. Orbital timing of the Indian, East Asian and African boreal monsoons and the concept of a "global monsoon." Quat. Sci. Rev. 30, 3705–3715.

Cantalejo, B., Pickering, K. T., 2015. Orbital forcing as principal driver for fine-grained deep-marine siliciclastic sedimentation, Middle-Eocene Ainsa Basin, Spanish Pyrenees. Palaeogeography, palaeoclimatology, palaeoecology, 421, 24-47.

Claussen, M., Kubatzki, C., Brovkin, V., Ganopolski, A., Hoelzmann, P., & Pachur, H. J., 1999. Simulation of an abrupt change in Saharan vegetation in the Mid-Holocene. Geophysical research letters, 26(14), 2037-2040.

Cochonat, P., 1998. ZAIANGO2 cruise, RV L'Atalante. doi:http://dx.doi.org/10.17600/98010110

Cochonat, P., 1993. GUINESS 2 cruise, RV Le Suroît. doi: https://doi.org/10.17600/93000190

Cochonat, P., Robin, A., 1992. GUINESS I cruise, RV L'Atalante. doi:http://dx.doi.org/10.17600/92004211

Csato, I., Granjeon, D., Catuneanu, O., Baum, G.R., 2013. A three-dimensional stratigraphic model for the Messinian crisis in the Pannonian Basin , eastern Hungary 121–148. doi:10.1111/j.1365-2117.2012.00553.x

Dalibard, M., Popescu, S.-M., Maley, J., Baudin, F., Melinte-Dobrinescu, M.-C., Pittet, B., Marsset, T., Dennielou, B., Droz, L., Suc, J.-P., 2014. High-resolution vegetation history of West Africa during the last 145 ka. Geobios 47, 183–198.

deMenocal, P.B., Rind, D., 1993. Sensitivity of Asian and African climate to variations in seasonal insolation, glacial ice cover, sea surface temperature, and Asian orography. J. Geophys. Res. Atmos. 98, 7265–7287.

Deville, E., Mascle, A., Callec, Y., Huyghe, P., Lallemant, S., Lerat, O., Mathieu, X., Carillo, C.P. De, Patriat, M., Pichot, T., Loubrieux, B., Granjeon, D., 2015. Tectonics and sedimentation interactions in the east Caribbean subduction zone : An overview from the Orinoco delta and the Barbados accretionary prism. Mar. Pet. Geol. 64, 76–103. doi:10.1016/j.marpetgeo.2014.12.015

Droz, L., Marsset, T., 2011. REPREZAI_LEG2 cruise, RV Le Suroît. doi:http://dx.doi.org/10.17600/11020020.

Droz, L., Marsset, T., Ondras, H., Lopez, M., Savoye, B., Spy-Anderson, F.-L., 2003. Architecture of an active mud-rich turbidite system: The Zaire Fan (Congo–Angola margin southeast Atlantic): Results from ZaAngo 1 and 2 cruises. Am. Assoc. Pet. Geol. Bull. 87, 1145–1168.

Droz, L., Rigaut, F., Cochonat, P., Tofani, R., 1996. Morphology and recent evolution of the Zaire turbidite system (Gulf of Guinea). Geol. Soc. Am. Bull. 108, 253–269.

Ducassou, E., Migeon, S., Mulder, T., Murat, A., Capotondi, L., Bernasconi, S.M., Mascle, J., 2009. Evolution of the Nile deep-sea turbidite system during the Late Quaternary: influence of climate change on fan sedimentation. Sedimentology 56, 2061–2090.

939 Dupont, L. (2011). Orbital scale vegetation change in Africa. Quaternary Science Reviews, 30(25-26), 3589-
940 3602.

941 Dupont, L.M., Behling, H., Jahns, S., Marret, F., Kim, J.-H., 2007. Variability in glacial and Holocene
942 marine pollen records offshore from west southern Africa. Veg. Hist. Archaeobot. 16, 87–100.

943 Dupont, L.M., Jahns, S., Marret, F., Ning, S., 2000. Vegetation change in equatorial West Africa: time-slices
944 for the last 150 ka. Palaeogeogr. Palaeoclimatol. Palaeoecol. 155, 95–122.

945 Dupont, L.M., Marret, F., Winn, K., 1998. Land-sea correlation by means of terrestrial and marine
946 palynomorphs from the equatorial East Atlantic: phasing of SE trade winds and the oceanic
947 productivity. Palaeogeogr. Palaeoclimatol. Palaeoecol. 142, 51–84.

948 Dypvik, H., Harris, N.B., 2001. Geochemical facies analysis of fine-grained siliciclastics using Th/U, Zr/Rb
949 and (Zr+ Rb)/Sr ratios. Chem. Geol. 181, 131–146.

950 Flood, R.D., Piper, D.J.W., 1997. Amazon fan sedimentation: the relationship to equatorial climate change,
951 continental denudation, and sea-level fluctuations, in: Proceedings-ocean drilling program scientific
952 results. National science foundation, pp. 653–675.

953 Foley, J.A., Kutzbach, J.E., Coe, M.T., Levis, S. 1994. Feedbacks between climate and boreal forests during
954 the Holocene epoch. Nature 371: 52-54.

955 Foucault, A., Powichrowski, L., Prud'homme, A., 1987. Le contrôle astronomique de la sédimentation
956 turbiditique: exemple du Flysch à Helminthoïdes des Alpes Ligures (Italie). Comptes Rendus de
957 l'Académie des Sciences, Paris, 305, 1007-1011.

958 Gaillardet, J., Dupré, B., Allègre, C.J., 1999. Geochemistry of large river suspended sediments: silicate
959 weathering or recycling tracer? Geochim. Cosmochim. Acta 63, 4037–4051.

960 Gaillardet, J., Dupré, B., Allègre, C.J., 1995. A global geochemical mass budget applied to the Congo Basin
961 rivers: erosion rates and continental crust composition. Geochim. Cosmochim. Acta 59, 3469–3485.

962 Galloway, W.E., 1998. Siliciclastic slope and base-of-slope depositional systems: component facies,
963 stratigraphic architecture, and classification. Am. Assoc. Pet. Geol. Bull. 82, 569–595.

964 Ganopolski, A., Kubatzki, C., Claussen, M., Brovkin, V., Petoukhov, V., 1998. The influence of vegetation-
965 atmosphere-ocean interaction on climate during the mid-Holocene. Science, 280(5371), 1916-1919.

966 Gasse, F., 2000. Hydrological changes in the African tropics since the Last Glacial Maximum. Quat. Sci.
967 Rev. 19, 189–211.

968 Gervais, V., Ducros, M., Granjeon, D., 2018. Probability maps of reservoir presence and sensitivity analysis
969 in stratigraphic forward modeling. AAPG Bulletin, 102(4), 613-628.

970 Gingele, F.X., Müller, P.M., Schneider, R.R., 1998. Orbital forcing of freshwater input in the Zaire Fan area
971 - clay mineral evidence from the last 200 kyr. Palaeogeogr. Palaeoclimatol. Palaeoecol. 138, 17–26.

972 Giresse, P., Wiewiora, A., Lacka, B., 1988. Mineral phases and processes within green peloids from two
973 recent 723 deposits near the Congo River mouth. Clay Minerals 23, 447–458.

974 Granjeon, D., 1997. Modelisation stratigraphique deterministe: conception et applications d'un modele
975 diffusif 3D multilithologique. PhD thesis. Université Rennes 1.

Granjeon, D., Joseph, P., 1999. Concepts and applications of a 3-D multiple lithology, diffusive model in stratigraphic modeling. SEPM Spec. Publ. 62, 197–210.

Granjeon, D., Joseph, P., Lafont, F., Guillocheau, F., 1994. Quantification de l'eustatisme haute-fréquence et de la subsidence par analyse de l'espace disponible. Application au bassin d'avant-pays sud-pyrénéen (région de Jaca, Eocène). Comptes rendus de l'Académie des sciences. Série 2, 319(9), 1071-1077.

Groenenberg, R. M., Hodgson, D. M., Prelat, A., Luthi, S. M., Flint, S. S., 2010. Flow–deposit interaction in submarine lobes: Insights from outcrop observations and realizations of a process-based numerical model. Journal of Sedimentary Research, 80(3), 252-267.

Groenenberg, R.M., Sloff, K., Weltje, G.J., 2009. A high-resolution 2-DH numerical scheme for process-based modeling of 3-D turbidite fan stratigraphy. Comput. Geosci. 35, 1686–1700.

Gvirtzman, Z., Csato, I., Granjeon, D., 2014. Constraining sediment transport to deep marine basins through submarine channels: The Levant margin in the Late Cenozoic. Mar. Geol. 347, 12–26.

Hatin, T., Crosta, X., Le Hérissé, A., Droz, L., Marsset, T., 2017. Diatom response to oceanographic and climatic 744 changes in the Congo fan area, equatorial Atlantic Ocean, during the last 190 ka BP. Palaeogeogr., 745 Palaeoclimato., Palaeoecol. 469, 47-59.

Hawie, N., Marfisi, E., Saint-Ange, F., MacDonald, A. W. A., 2019. Statistical analysis of forward stratigraphic models in complex salt provinces: The central Scotian Basin case study. AAPG Bulletin, 103(2), 433-467.

Hawie, N., Covault, J. A., Dunlap, D., Sylvester, Z., 2018. Slope-fan depositional architecture from high-resolution forward stratigraphic models. Marine and Petroleum Geology, 91, 576-585.

Heard, T. G., Pickering, K. T., & Robinson, S. A., 2008. Milankovitch forcing of bioturbation intensity in deep-marine thin-bedded siliciclastic turbidites. Earth and Planetary Science Letters, 272(1-2), 130-138.

Heezen, B.C., Menzies, R.J., Schneider, E.D., Ewing, W.M., Granelli, N.C.L., 1964. Congo submarine canyon. Am. Assoc. Pet. Geol. Bull. 48, 1126–1149.

Hodgson, D.M., Flint, S.S., Hodgetts, D., Drinkwater, N.J., Johannessen, E.P., Luthi, S.M., 2006. Stratigraphic evolution of fine-grained submarine fan systems, Tanqua depocenter, Karoo Basin, South Africa. J. Sediment. Res. 76, 20–40.

Holtvoeth, J., Wagner, T., Horsfield, B., Schubert, C., Wand, U., 2001. Late-Quaternary supply of terrigenous organic matter to the Congo deep-sea fan (ODP site 1075): implications for equatorial African paleoclimate. Geo-Marine Lett. 21, 23–33.

Hoorn, C., Guerrero, J., Sarmiento, A. S., Lorente, M. A. 1995. Andean tectonics as a cause for changing drainage pattern in Miocene northern South America. Geology, 23, 237-240.

Hou, J., Wang, H., Fu, B., Zhu, L., Wang, Y., Li, Z., 2016. Effects of plant diversity on soil erosion for different vegetation patterns. Catena 147, 632–637.

Jahns, S., 1996. Vegetation history and climate changes in West Equatorial Africa during the Late Pleistocene and Holocene, based on a marine pollen diagram from the Congo fan. Veg. Hist. Archaeobot. 5, 207–213.

Jahns, S., Hüls, M., Sarnthein, M., 1998. Vegetation and climate history of west equatorial Africa based on a marine pollen record off Liberia (site GIK 16776) covering the last 400,000 years. Rev. Palaeobot. Palynol. 102, 277–288.

Kane, I. A., Clare, M. A, 2019. Dispersion, accumulation and the ultimate fate of microplastics in deep-marine environments: A review and future directions. Frontiers in Earth Science, 7, 80.

Kaufman, P., Grotzinger, J.P., McCormick, D.S., 1991. Depth-dependent diffusion algorithm for simulation of sedimentation in shallow marine depositional systems. Kansas Geol. Surv. Bull. 233, 489–508.

Kettner, A. J., Syvitski, J. P., 2008. HydroTrend v. 3.0: A climate-driven hydrological transport model that simulates discharge and sediment load leaving a river system. Computers & Geosciences, 34(10), 1170-1183.

Khripounoff, A., Vangriesheim, A., Babonneau, N., Crassous, P., Dennielou, B., Savoye, B., 2003. Direct observation of intense turbidity current activity in the Zaire submarine valley at 4000 m water depth. Mar. Geol. 194, 151–158.

Kneller, B., 2003. The influence of flow parameters on turbidite slope channel architecture. Marine and Petroleum Geology, 20(6-8), 901-910.

Kolla, V., 2007. A review of sinuous channel avulsion patterns in some major deep-sea fans and factors controlling them. Mar. Pet. Geol. 24, 450–469.

Krom, M.D., Stanley, J.D., Cliff, R.A., Woodward, J.C., 2002. Nile River sediment fluctuations over the past 7000 yr and their key role in sapropel development. Geology 30, 71–74.

Kutzbach, J., Bonan, G., Foley, J., Harrison, S.P., 1996. Vegetation and soil feedbacks on the response of the African monsoon to orbital forcing in the early to middle Holocene. Nature 384, 623.

Labourdette, R., Bez, M., 2010. Element migration in turbidite systems: Random or systematic depositional processes?. AAPG bulletin, 94(3), 345-368.

Lai, S.Y.J., Capart, H., 2007. Two-diffusion description of hyperpycnal deltas. J. Geophys. Res. Earth Surf. 112.

Laraque, A., Bellanger, M., Adele, G., Guebanda, S., Gulemvuga, G., Pandi, A., Paturel, J.E., Robert, A., Tathy, J.P., Yambélé, A., 2013. Evolutions récentes des débits du Congo, de l'Oubangui et de la Sangha. Geo-Eco Trop 37, 93–100.

Laraque, A., Bricquet, J.P., Pandi, A., Olivry, J.C., 2009. A review of material transport by the Congo River and its tributaries. Hydrol. Process. 23, 3216–3224.

Laraque, A., Moukolo, N., Olivry, J.C., Bricquet, J.P., 1993. Transport en solution et en suspension par le fleuve Congo (Zaïre) et ses principaux affluents de la rive droite. Hydrol. Sci. J. 38, 133–145.

Lavier, L.L., Steckler, M.S., Brigaud, F., 2001. Climatic and tectonic control on the Cenozoic evolution of the West African margin. Mar. Geol. 178, 63–80.

Lavier, L.L., Steckler, M.S., Brigaud, F., 2000. An improved method for reconstructing the stratigraphy and bathymetry of continental margins: Application to the Cenozoic tectonic and sedimentary history of the Congo margin. Am. Assoc. Pet. Geol. Bull. 84, 923–939.

Ledru, M., Salatino, M.L.F., Ceccantini, G., Salatino, A., Pinheiro, F., Pintaud, J., 2007. Regional assessment of the impact of climatic change on the distribution of a tropical conifer in the lowlands of South America. Divers. Distrib. 13, 761–771.

Leroux, E., Rabineau, M., Aslanian, D., Granjeon, D., Droz, L., Gorini, C., 2014. Stratigraphic simulations of the shelf of the Gulf of Lions : testing subsidence rates and sea-level curves during the Pliocene and Quaternary. doi:10.1111/ter.12091

Leroux, M., 1993. The Mobile Polar High: a new concept explaining present mechanisms of meridional air-mass and energy exchanges and global propagation of palaeoclimatic changes. Glob. Planet. Change 7, 69–93.

Lisiecki, L.E., Raymo, M.E., 2005. A Pliocene-Pleistocene stack of 57 globally distributed benthic δ18O records. Paleoceanography 20.

Lopez, M., 2001. Architecture and depositional pattern of the Quaternary deep-sea fan of the Amazon. Mar. Pet. Geol.18, 479–486.

Marret, F., Scourse, J., Jansen, J.H.F., Schneider, R., 1999. Changements climatiques et paléocéanographiques en Afrique centrale atlantique au cours de la dernière déglaciation: contribution palynologique. Comptes Rendus l'Académie des Sci. IIA-Earth Planet. Sci. 329, 721–726.

Marsset, T., Droz, L., 2010. REPREZAI_LEG1 cruise, RV Pourquoi pas ?. doi:http://dx.doi.org/10.17600/10030170

Marsset, T., Droz, L., Dennielou, B., Pichon, E., 2009. Cycles in the architecture of the Quaternary Zaire turbidite system: a possible link with climate. Extern. Control. Deep. Depos. Syst. SEPM, Spec. Publ. 92, 89–106.

Martins, O., Probst, J.L., 1991. Biogeochemistry of major African rivers: carbon and mineral transport, in: Degens, E.., Kempe, S., Richey, J.. (Eds.), Biogeochemical of Major World Rivers. pp. 127–156.

Maslin, M., Knutz, P. C., Ramsay, T. (2006). Millennial-scale sea-level control on avulsion events on the Amazon Fan. Quaternary Science Reviews, 25(23-24), 3338-3345.

Michalopoulos, P., Aller, R.C., 2004. Early diagenesis of biogenic silica in the Amazon delta : Alteration, 839 authigenic clay formation, and storage. Geochimica and Cosmochimica Acta 68, 1061-1085.

Milliman, J. D., Syvitski, J. P., 1992. Geomorphic/tectonic control of sediment discharge to the ocean: the importance of small mountainous rivers. The Journal of Geology, 525-544.

Mitchell, N.C., Huthnance, J.M., 2008. Oceanographic currents and the convexity of the uppermost continental slope. J. Sediment. Res. 78, 29–44.

Moguedet, G., 1988. Les relations entre le fleuve congo et la sedimentation recente sur la marge continentale entre l'embouchure et le sud du gabon: etude hydrologique, sedimentologique et geochimique. PhD thesis, University of Angers.

Molliex, S., Kettner, A. J., Laurent, D., Droz, L., Marsset, T., Laraque, Rabineau, M., N'Kaya, G. D. M., 2019. Simulating sediment supply from the Congo watershed over the last 155 ka. Quaternary Science Reviews, 203, 38-55.

Mutti, E., Normark, W.R., 1987. Comparing examples of modern and ancient turbidite systems: problems and concepts, in: Marine Clastic Sedimentology. Springer, pp. 1–38.

Nygard, R., Gutierrez, M., Gautam, R., Hoeg, K., 2004. Compaction behavior of argillaceous sediments as function of diagenesis. Mar. Pet. Geol. 21, 349–362.

Nze Abeigne, C.R., 1997. Evolution post-rift de la marge continentale Sud-Gabon: contrôles tectonique et climatique sur la sédimentation. PhD thesis, University of Montpellier 2.

Ortiz-Karpf, A., Hodgson, D. M., McCaffrey, W. D., 2015. The role of mass-transport complexes in controlling channel avulsion and the subsequent sediment dispersal patterns on an active margin: the Magdalena Fan, offshore Colombia. Marine and Petroleum Geology, 64, 58-75.

Paola, C., Heller, P.L., Angevine, C.L., 1992. The large-scale dynamics of grain-size variation in alluvial basins, 1: Theory. Basin Res. 4, 73–90.

Picot, M., Marsset, T., Droz, L., Dennielou, B., Baudin, F., Hermoso, De Rafelis, M., Sionneau, T., Cremer, M., Laurent, D., Bez, M., 2019. Monsoon control on channel avulsions in the Late Quaternary Congo Fan. Quaternary Science Reviews, 204, 149-171.

Picot, M., Droz, L., Marsset, T., Dennielou, B., Bez, M., 2016. Controls on turbidite sedimentation: Insights from a quantitative approach of submarine channel and lobe architecture (Late Quaternary Congo Fan). Mar. Pet. Geol. 72, 423–446.

Pirmez, C., Hiscott, R.N., Kronen, J.D., 1997. Sandy turbidite successions at the base of channel-levee systems of the Amazon Fan revealed by FMS logs and cores: unraveling the facies architecture of large submarine fans, in: Proceedings of the Ocean Drilling Program. Scientific Results. Ocean Drilling Program, pp. 7–33.

Posamentier, H.W., Kolla, V., 2003. Seismic geomorphology and stratigraphy of depositional elements in deep-water settings. J. Sediment. Res. 73, 367–388.

Posamentier, H.W., Erskine, R.D., Jr, R.M.M., 1991. Models for Submarine-Fan Deposition within a Sequence- Stratigraphic Framework, in: Weimer, P., Link, M.H. (Eds.), Seismic Facies and Sedimentary Processes of Submarine Fans and Turbidite Systems, Frontiers in Sedimentary Geology. Springer New York, pp. 127–136.

Prather, B.E., Booth, J.R., Steffens, G.S., Craig, P.A., 1998. Classification, Lithologic Calibration, and Stratigraphic Succession of Seismic Facies of Intraslope Basins, Deep-Water Gulf of Mexico. AAPG Bull. 82, 701–728.

Rabineau, M., Berné,S., Aslanian, D., Olivet J-L., Joseph, P, Guillocheau, F, Bourillet, J-F., Ledrezen, E., Granjeon, D., 2005: Sedimentary sequences in the Gulf of Lions: a record of 100,000 years climatic cycles, Marine and Petroleum Geology, 22, p. 775-804).

Rabouille, C., Dennielou, B., Baudin, F., Raimonet, M., Droz, L., Khripounoff, A., Martinez, P., Mejanelle, L., Michalopoulos, P., Pastor, L., Pruski, A., Ragueneau, O., Reyss, J-L., Ruffine, L., J.Schnyder, J., Stetten, E., Taillefert, M., Tourolle, J., Olu, K., 2019. Carbon and silica megasink in deep-sea sediments of the Congo terminal lobes. Quaternary Science Reviews, 222, 105854.

Reading, H.G., Richards, M., 1994. Turbidite systems in deep-water basin margins classified by grain size and feeder system. Am. Assoc. Pet. Geol. Bull. 78, 792–822.

Renard, K.G., Foster, G.R., Weesies, G.A., McCool, D.K., Yoder, D.C., 1997. Predicting soil erosion by water: a guide to conservation planning with the Revised Universal Soil Loss Equation (RUSLE). US Government Printing Office Washington, DC.

Sangster, C., Piper, D. J., Hawie, N., Pe-Piper, G., Saint-Ange, F., 2019. Forward stratigraphic modelling of sediment pathways and depocentres in salt-influenced passive-margin basins: Lower Cretaceous, central Scotian Basin. Basin Research, 31(4), 728-753.

Savoye, B., 1998. ZAIANGO1 cruise, RV L'Atalante. doi:http://dx.doi.org/10.17600/98010100

Savoye, B., Babonneau, N., Dennielou, B., Bez, M., 2009. Geological overview of the Angola–Congo margin, the Congo deep-sea fan and its submarine valleys. Deep Sea Res. Part II Top. Stud. Oceanogr. 56, 2169–2182.

Savoye, B., Cochonat, P., Apprioual, R., Bain, O., Baltzer, A., Bellec, V., Beuzart, P., Bourillet, J.-F., Cagna, R., Cremer, M., 2000. Structure et évolution récente de l'éventail turbiditique du Zaïre: premiers résultats scientifiques des missions d'exploration Zaïango1 & 2 (marge Congo–Angola). Comptes Rendus l'Académie des Sci. IIA-Earth Planet. Sci. 331, 211–220.

Schneider, R.R., Price, B., Müller, P.J., Kroon, D., Alexander, I., 1997. Monsoon related variations in Zaire (Congo) sediment load and influence of fluvial silicate supply on marine productivity in the east equatorial Atlantic during the last 200,000 years. Paleoceanography 12, 463–481.

Scotchman, J. I., Pickering, K. T., Sutcliffe, C., Dakin, N., Armstrong, E., 2015. Milankovitch cyclicity within the middle Eocene deep-marine Guaso system, Ainsa Basin, Spanish Pyrenees. Earth-Science Reviews, 144, 107-121.

Seard, C., Borgomano, J., Granjeon, D., Camoin, G., 2013. Impact of environmental parameters on coral reef development and drowning: Forward modelling of the last deglacial reefs from Tahiti (French Polynesia; IODP Expedition# 310). Sedimentology 60, 1357–1388.

Sionneau, T., Droz, L., Marsset, T., Dennielou, B., Bez, M., 2010. Congo-Zaire detrital supply variability during the last 200 ka: a possible explanation for the longitudinal migration of the Zaire fan depocenters. International Sedimentological Congress, 2010, Mendoza (Argentine).

Sømme, T.O., Helland-Hansen, W., Martinsen, O.J., Thurmond, J.B., 2009. Relationships between morphological and sedimentological parameters in source-to-sink systems: a basis for predicting semi-quantitative characteristics in subsurface systems. Basin Res. 21, 361–387.

Spratt, R. M., Lisiecki, L. E. (2016). A Late Pleistocene sea level stack. Climate of the Past, 12(4), 1079-1092.

Steckler, M.S., Mountain, G.S., Miller, K.G., Christie-Blick, N., 1999. Reconstruction of Tertiary progradation and clinoform development on the New Jersey passive margin by 2-D backstripping. Mar. Geol. 154, 399–420.

Stouthamer, E., Berendsen, H. J., 2007. Avulsion: the relative roles of autogenic and allogenic processes. Sedimentary Geology, 198(3-4), 309-325.

Summerfield, M.A., Hulton, N.J., 1994. Natural controls of fluvial denudation rates in major world drainage basins. J. Geophys. Res. Ser. 99, 13–871.

1164 Syvitski, J.P.M., Milliman, J.D., 2007. Geology, geography, and humans battle for dominance over the
1165 delivery of fluvial sediment to the coastal ocean. J. Geol. 115, 1–19.

1166 Syvitski, J.P.M., Peckham, S.D., Hilberman, R., Mulder, T., 2003. Predicting the terrestrial flux of sediment
1167 to the global ocean: a planetary perspective. Sediment. Geol. 162, 5–24.

1168 Syvitski, J. P., Morehead, M. D., Nicholson, M., 1998. HYDROTREND: a climate-driven hydrologic-
1169 transport model for predicting discharge and sediment load to lakes or oceans. Computers &
1170 Geosciences, 24(1), 51-68.

1171 Toucanne, S., Zaragosi, S., Bourillet, J. F., Dennielou, B., Jorry, S. J., Jouet, G., & Cremer, M., 2012.
1172 External controls on turbidite sedimentation on the glacially-influenced Armorican margin (Bay of
1173 Biscay, western European margin). Marine Geology, 303, 137-153.

1174 Toucanne, S., Zaragosi, S., Bourillet, J. F., Naughton, F., Cremer, M., Eynaud, F., Dennielou, B., 2008.
1175 Activity of the turbidite levees of the Celtic–Armorican margin (Bay of Biscay) during the last 30,000
1176 years: imprints of the last European deglaciation and Heinrich events. Marine Geology, 247(1-2), 84-
1177 103.

1178 Turakiewicz, G., 2004. Les mécanismes forçants dans les éventails turbiditiques de marges matures: exemple
1179 de l'éventail quaternaire du Congo. PhD thesis, University of Montpellier 2.

1180 Van Weering, T.C.E., Van Iperen, J., 1984. Fine-grained sediments of the Zaire deep-sea fan, southern
1181 Atlantic Ocean. Geol. Soc. London, Spec. Publ. 15, 95–113.

1182 Weber, M.E., Wiedicke-Hombach, M., Kudrass, H.R., Erlenkeuser, H., 2003. Bengal Fan sediment transport
1183 activity and response to climate forcing inferred from sediment physical properties. Sediment. Geol.
1184 155, 361–381.

1185 Wefer, G., Berger, W.H., Richter, C., 1998. Facies patterns and authigenic minerals of upwelling deposits off
1186 Southwest Africa, in: Proceedings of the Ocean Drilling Program. Initial Reports. Ocean Drilling
1187 Program, pp. 487–504.

1188 Weldeab, S., Lea, D.W., Schneider, R.R., Andersen, N., 2007. 155,000 years of West African monsoon and
1189 ocean thermal evolution. Science (80). 316, 1303–1307.

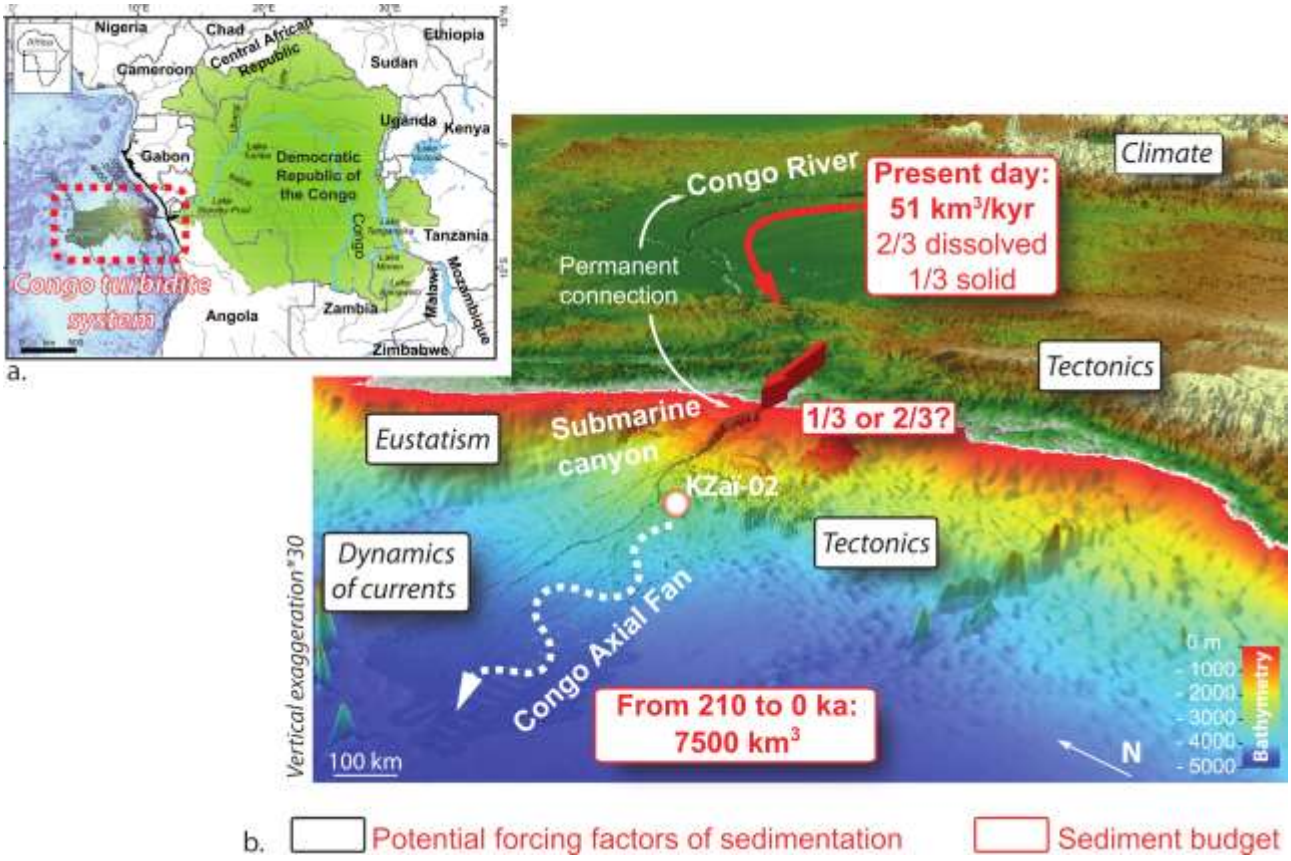
1190 Weltje, G., de Boer, P. L., 1993. Astronomically induced paleoclimatic oscillations reflected in Pliocene
1191 turbidite deposits on Corfu (Greece): implications for the interpretation of higher order cyclicity in
1192 ancient turbidite systems. Geology, 21(4), 307-310.

1193 Zabel, M., Schneider, R.R., Wagner, T., Adegbie, A.T., de Vries, U., Kolonic, S., 2001. Late Quaternary
1194 climate changes in Central Africa as inferred from terrigenous input to the Niger Fan. Quat. Res. 56,
1195 207–217.

1196 Zhou, P., Luukkanen, O., Tokola, T., Nieminen, J., 2008. Effect of vegetation cover on soil erosion in a
1197 mountainous watershed. Catena 75, 319–325.

1198

1199



1200

Figure 1

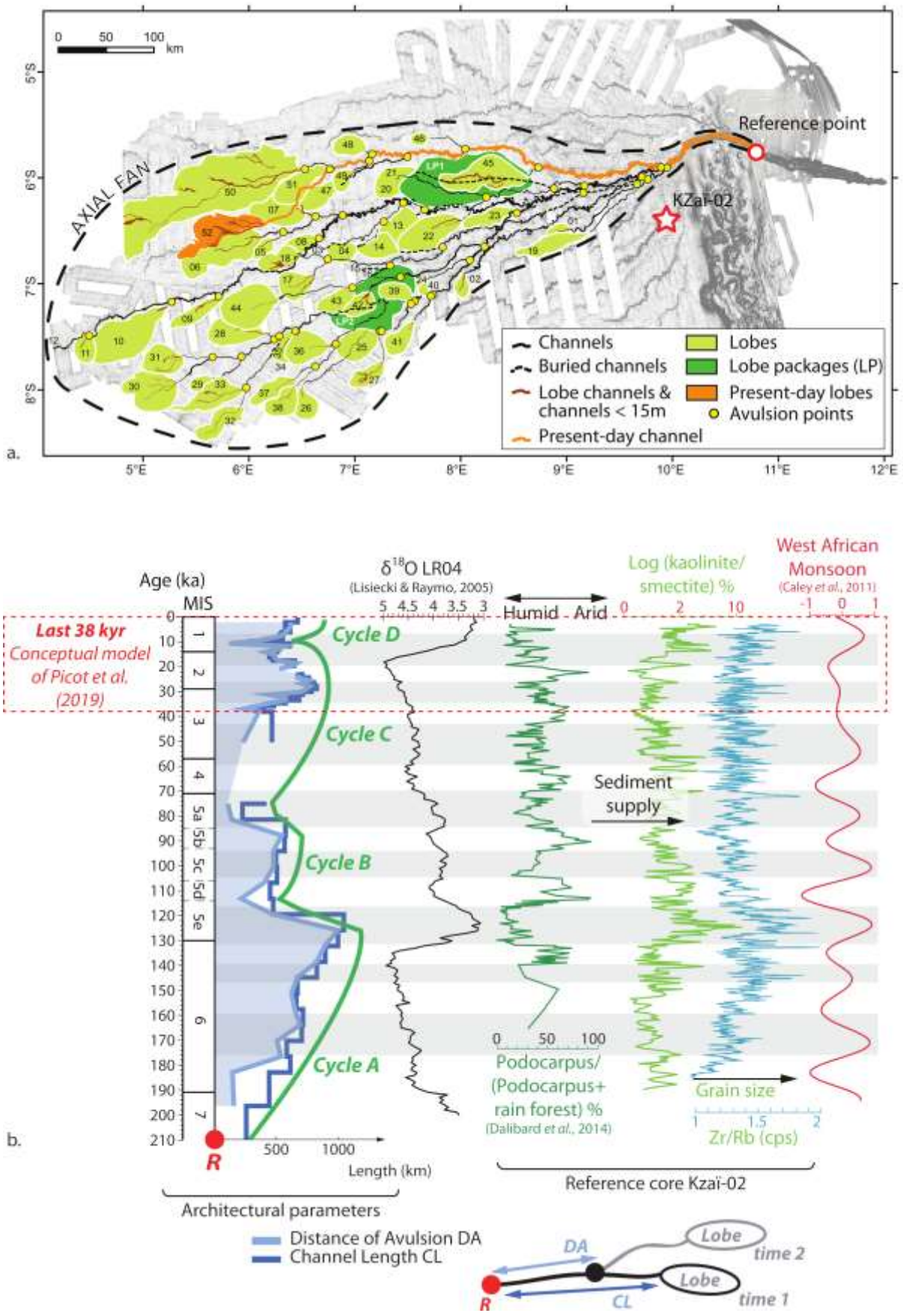

a.
0 50 100 km
5°S
6°S
7°S
8°S
5°E
6°E
7°E
8°E
9°E
10°E
11°E
12°E
AXIAL FAN
Reference point
KZaï-02
Channels
Buried channels
Lobe channels & channels < 15m
Present-day channel
Lobes
Lobe packages (LP)
Present-day lobes
Avulsion points
b.
Age (ka)
MIS
Last 38 kyr
Conceptual model of Picot et al. (2019)
δ18O LR04
(Lisiecki & Raymo, 2005)
Humid
Arid
Log (kaolinite/ smectite) %
West African Monsoon
(Caley et al., 2011)
Cycle D
Cycle C
Cycle B
Cycle A
Sediment supply
Podocarpus/ (Podocarpus+ rain forest) %
(Dalibard et al., 2014)
Grain size
Zr/Rb (cps)
R
Length (km)
Architectural parameters
Distance of Avulsion DA
Channel Length CL
Reference core Kzaï-02
DA
CL
Lobe time 2
Lobe time 1

Figure 2

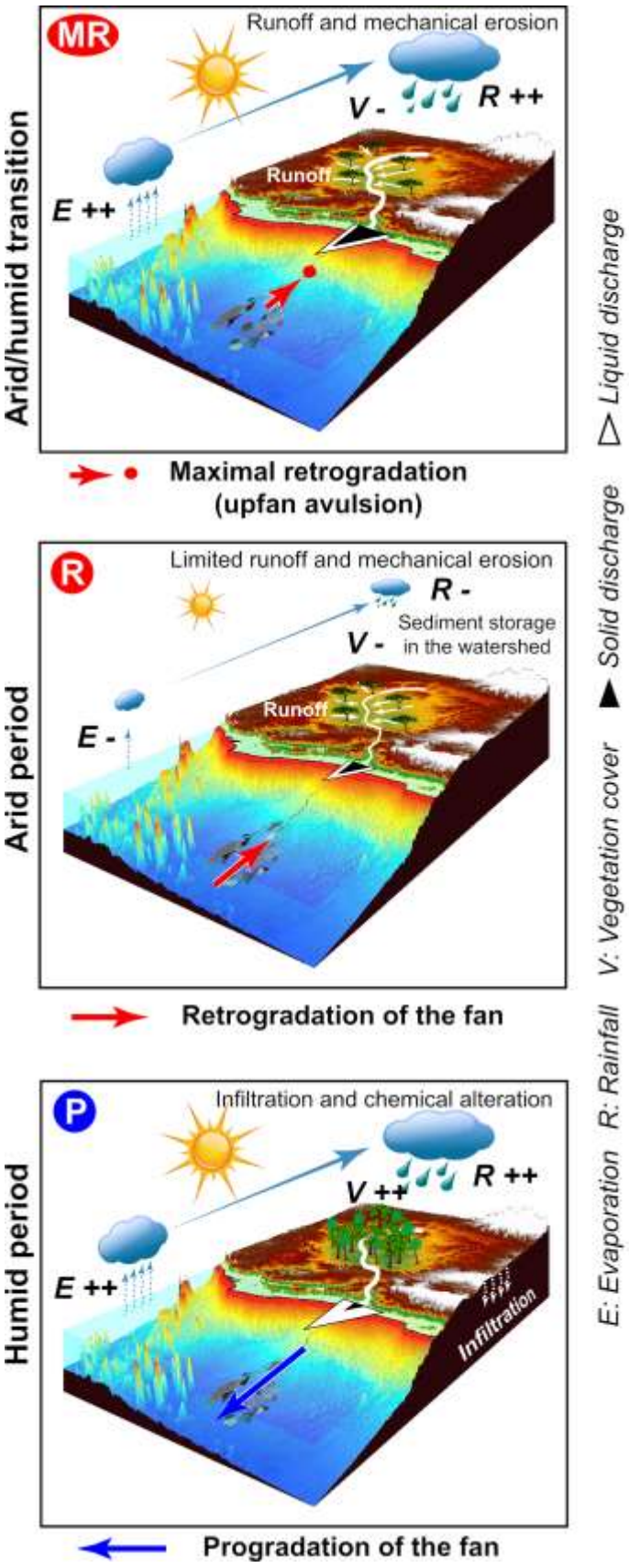

MR
Runoff and mechanical erosion
V -
R ++
Runoff
E ++
Arid/humid transition
Maximal retrogradation
(upfan avulsion)
R
Limited runoff and mechanical erosion
R -
Sediment storage
in the watershed
V -
Runoff
E -
Arid period
Retrogradation of the fan
P
Infiltration and chemical alteration
V ++
R ++
E ++
Infiltration
Humid period
Progradation of the fan
E: Evaporation R: Rainfall V: Vegetation cover
▲ Solid discharge
▷ Liquid discharge

Figure 3

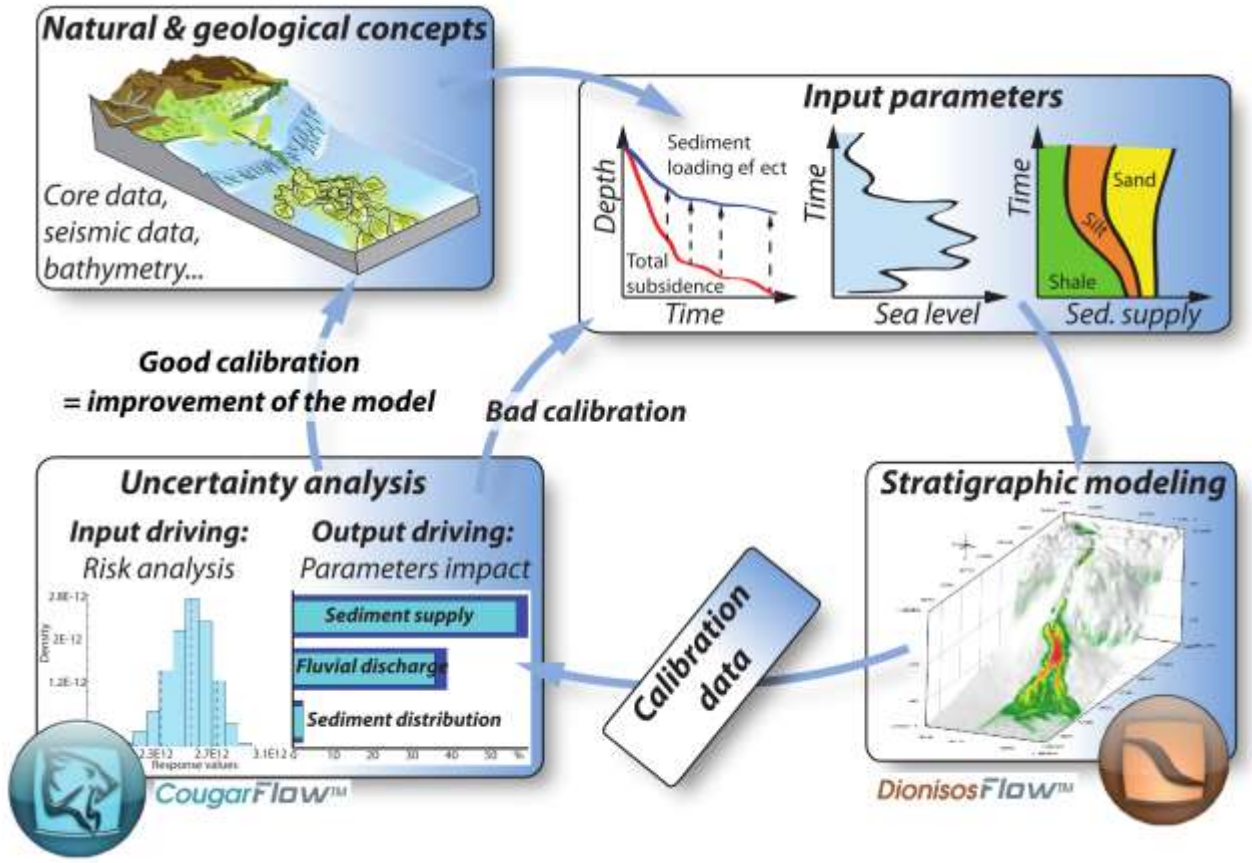
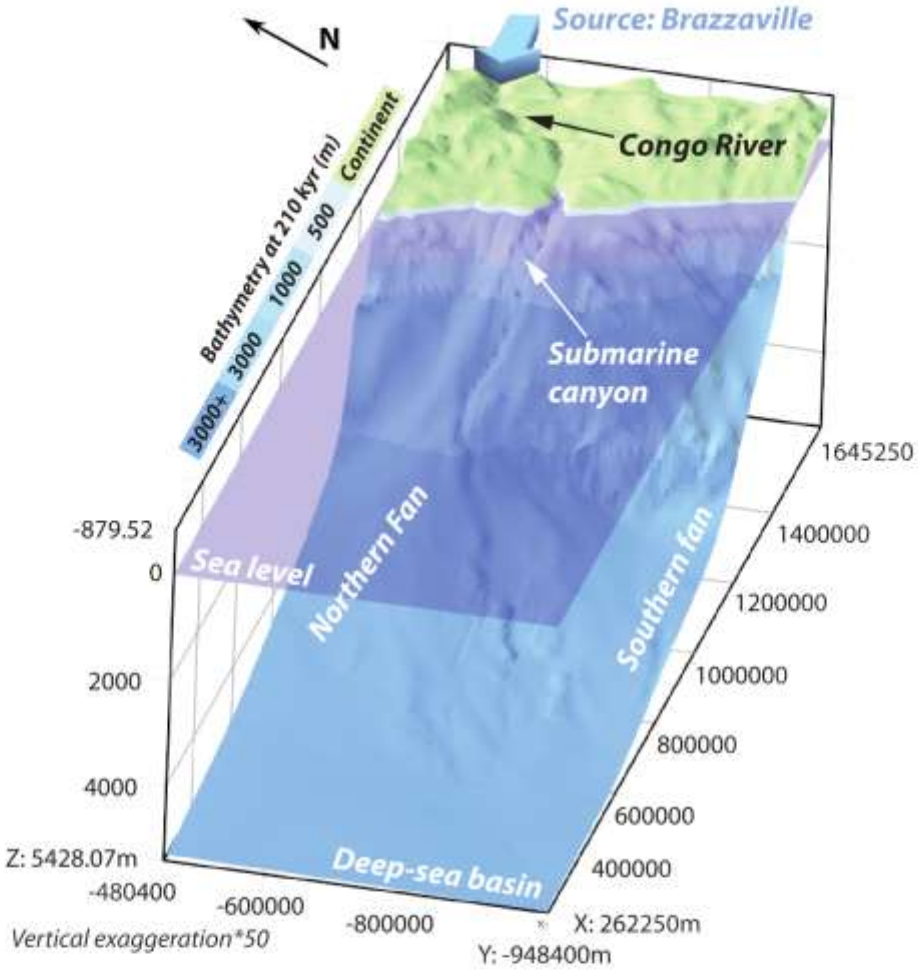

Natural & geological concepts
Core data,
seismic data,
bathymetry...
Input parameters
Depth
Sediment
loading ef ect
Total
subsidence
Time
Time
Sea level
Time
Sand
Silt
Shale
Sed. supply
Good calibration
= improvement of the model
Bad calibration
Uncertainty analysis
Input driving:
Risk analysis
Output driving:
Parameters impact
Sediment supply
Fluvial discharge
Sediment distribution
CougarFlow™
Calibration
data
Stratigraphic modeling
DionisosFlow™

Figure 4



Model characteristics

Display time: from 210 to 0 ka
Time step: 5 kyr
Model size: 1383*468 km^2
Cell dimension: 6*6 km^2
Model boundaries: closed

Source characteristics

	Qw (.10^3 m^3/s):	Qs (.10^3 km^3/Myr):
Mean	41	37
Glacial periods	Between 18 & 65	Between 24 & 46
Interglacial periods		Between 32 & 62

Lithologies: sand and mud (compaction laws by default)

Sand/(sand+mud) - Glacial periods: 24%
Interglacial periods: 30%

Sea level variation: LR04 *(Spratt and Lisiecki, 2016)*

No subsidence

Diffusion coefficients K (constant over time)

	Sand	Mud
Gravity-driven $K_{gravity}$		
Continental (km^2/kyr)	0.001	0.001
Marine (km^2/kyr)	0.01	0.01
Water-driven K_{water}		
Continental (km^2/kyr)	100	100
Marine (km^2/kyr)	1.5	10
High-energy short-term: K_{hest}		
Continental (km^2/kyr)	100	100
Marine (km^2/kyr)	1.5	10

Figure 5

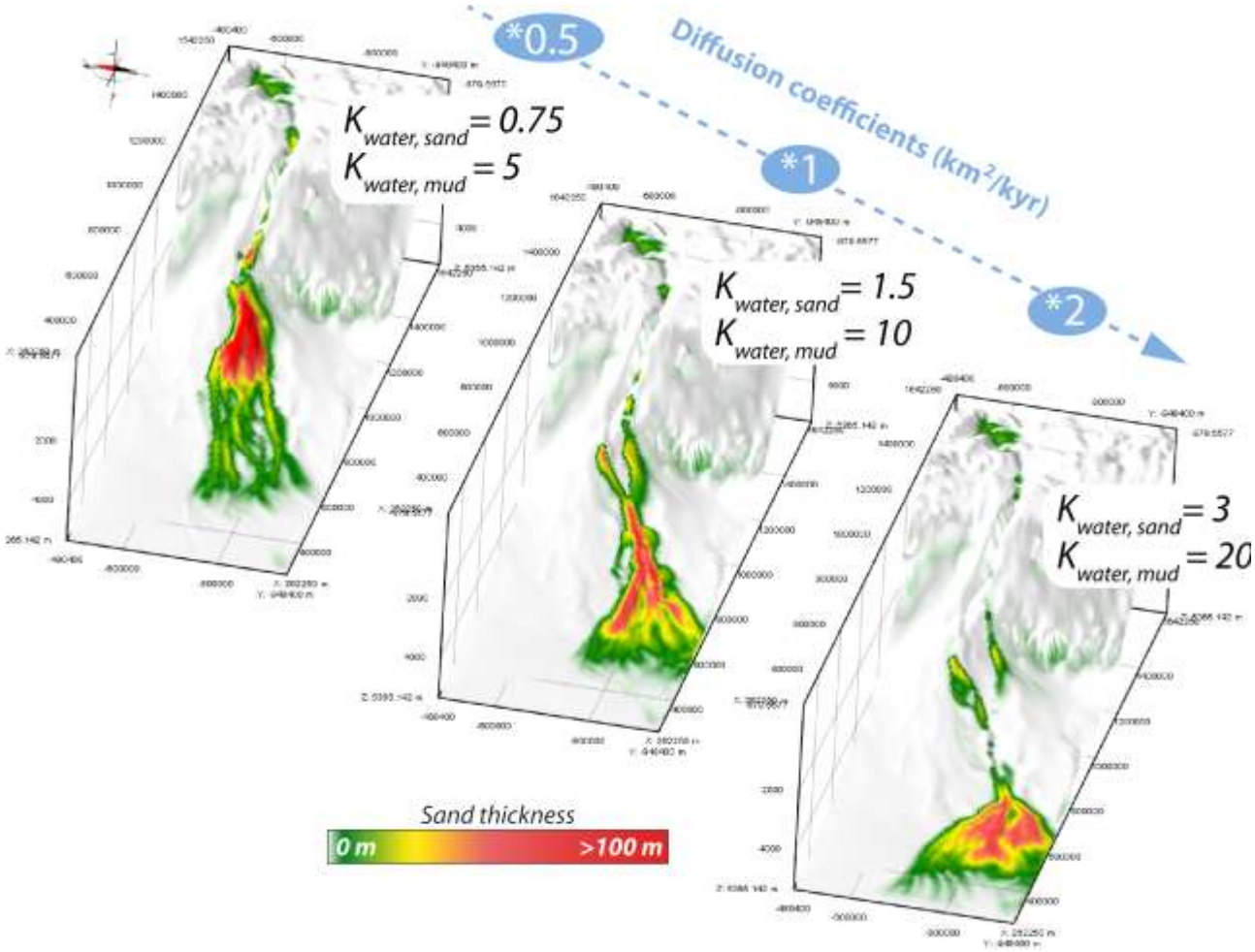

*0.5
Diffusion coefficients (km²/kyr)
*1
*2
K water, sand = 0.75
K water, mud = 5
K water, sand = 1.5
K water, mud = 10
K water, sand = 3
K water, mud = 20
Sand thickness
0 m
>100 m

Figure 6

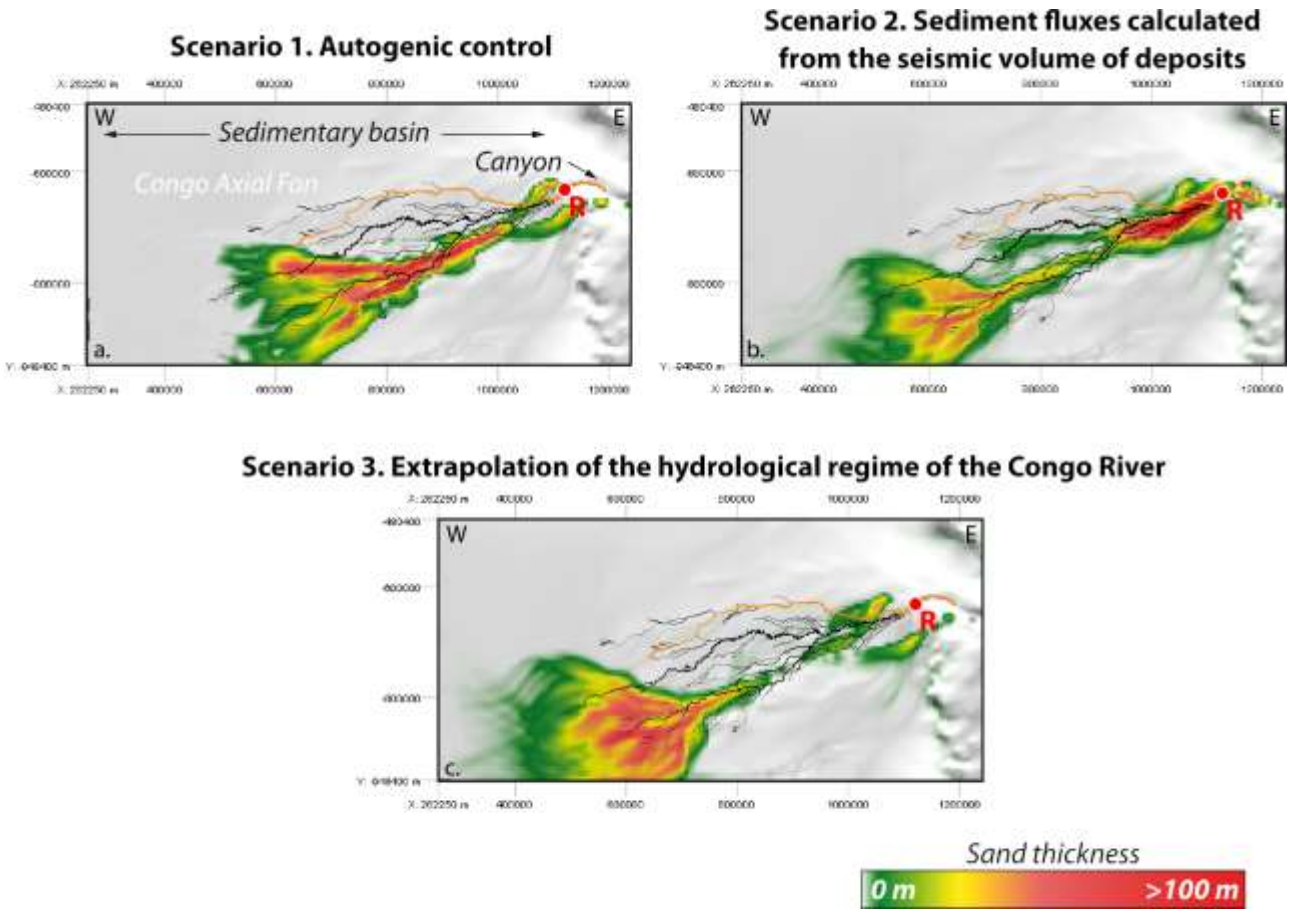

Scenario 1. Autogenic control
W
E
Sedimentary basin
Canyon
Congo Axial Fan
R
a.
Scenario 2. Sediment fluxes calculated from the seismic volume of deposits
W
E
R
b.
Scenario 3. Extrapolation of the hydrological regime of the Congo River
W
E
R
c.
Sand thickness
0 m
>100 m

Figure 7

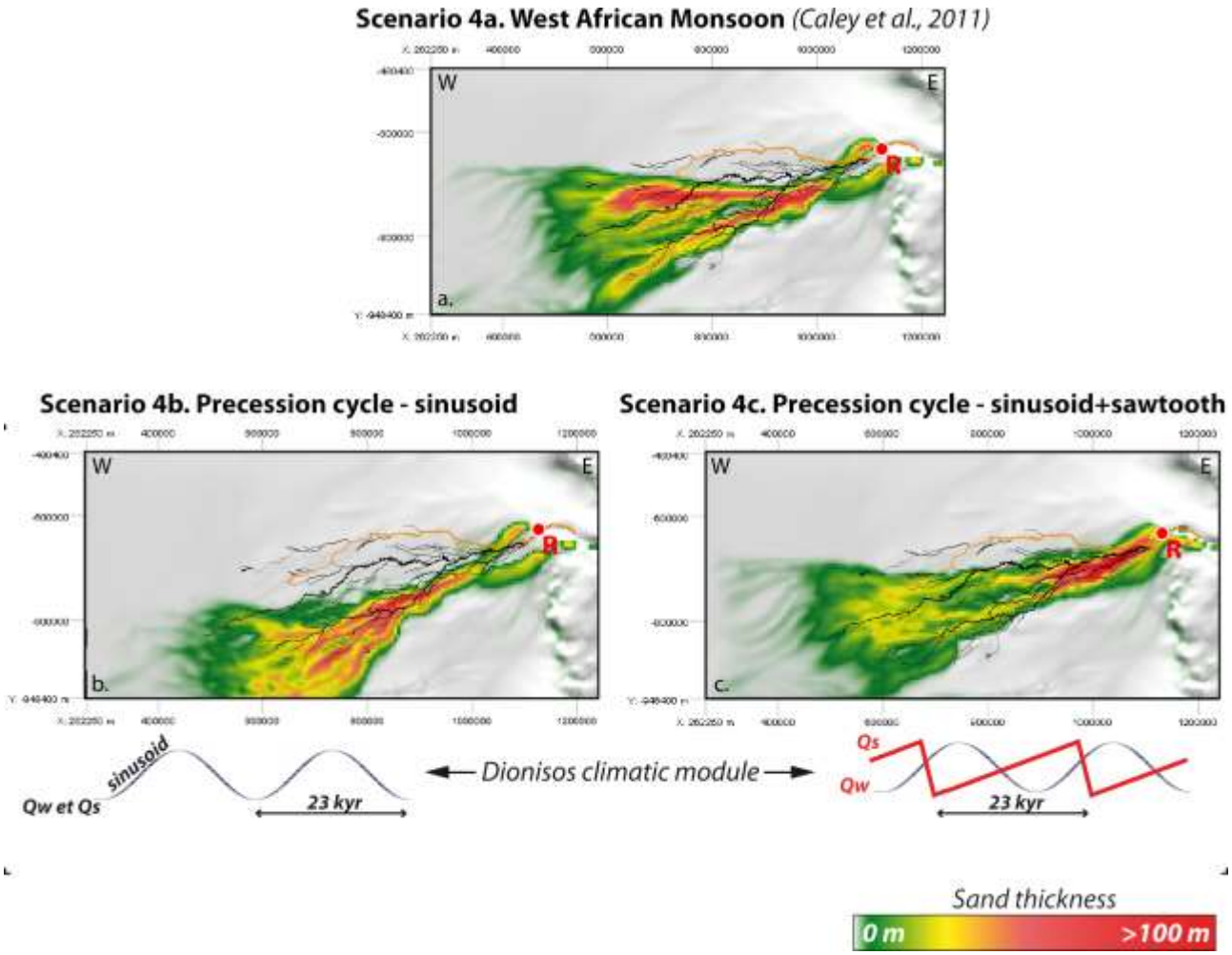

Scenario 4a. West African Monsoon (Caley et al., 2011)
W
E
R
a.
Scenario 4b. Precession cycle - sinusoid
b.
Scenario 4c. Precession cycle - sinusoid+sawtooth
c.
sinusoid
Qw et Qs
23 kyr
Dionisos climatic module
Qs
Qw
23 kyr
Sand thickness
0 m
>100 m

Figure 8

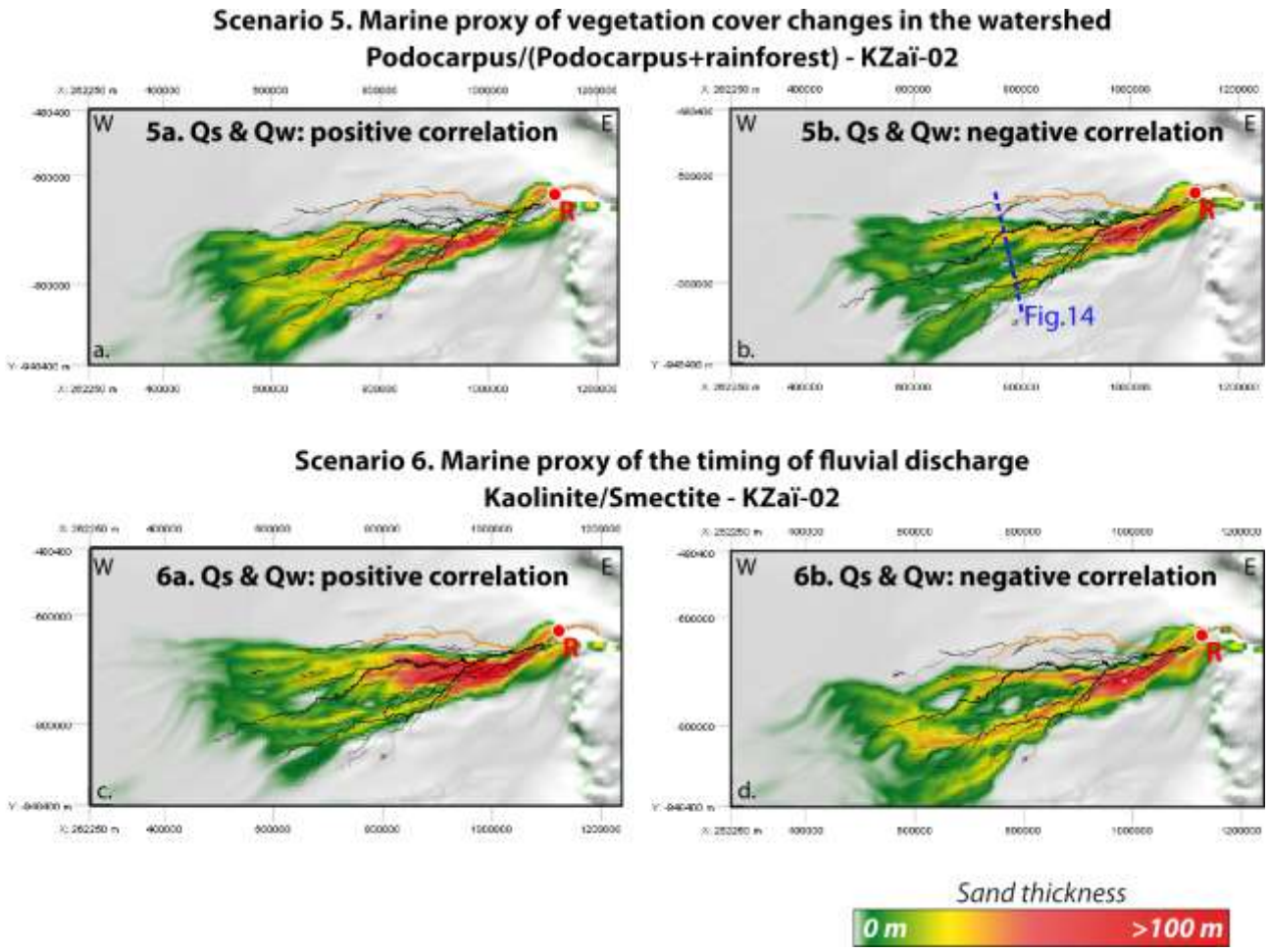

Scenario 5. Marine proxy of vegetation cover changes in the watershed
Podocarpus/(Podocarpus+rainforest) - KZaï-02
W
E
5a. Qs & Qw: positive correlation
R
a.
5b. Qs & Qw: negative correlation
Fig.14
b.
Scenario 6. Marine proxy of the timing of fluvial discharge
Kaolinite/Smectite - KZaï-02
6a. Qs & Qw: positive correlation
c.
6b. Qs & Qw: negative correlation
d.
Sand thickness
0 m
>100 m

Figure 9

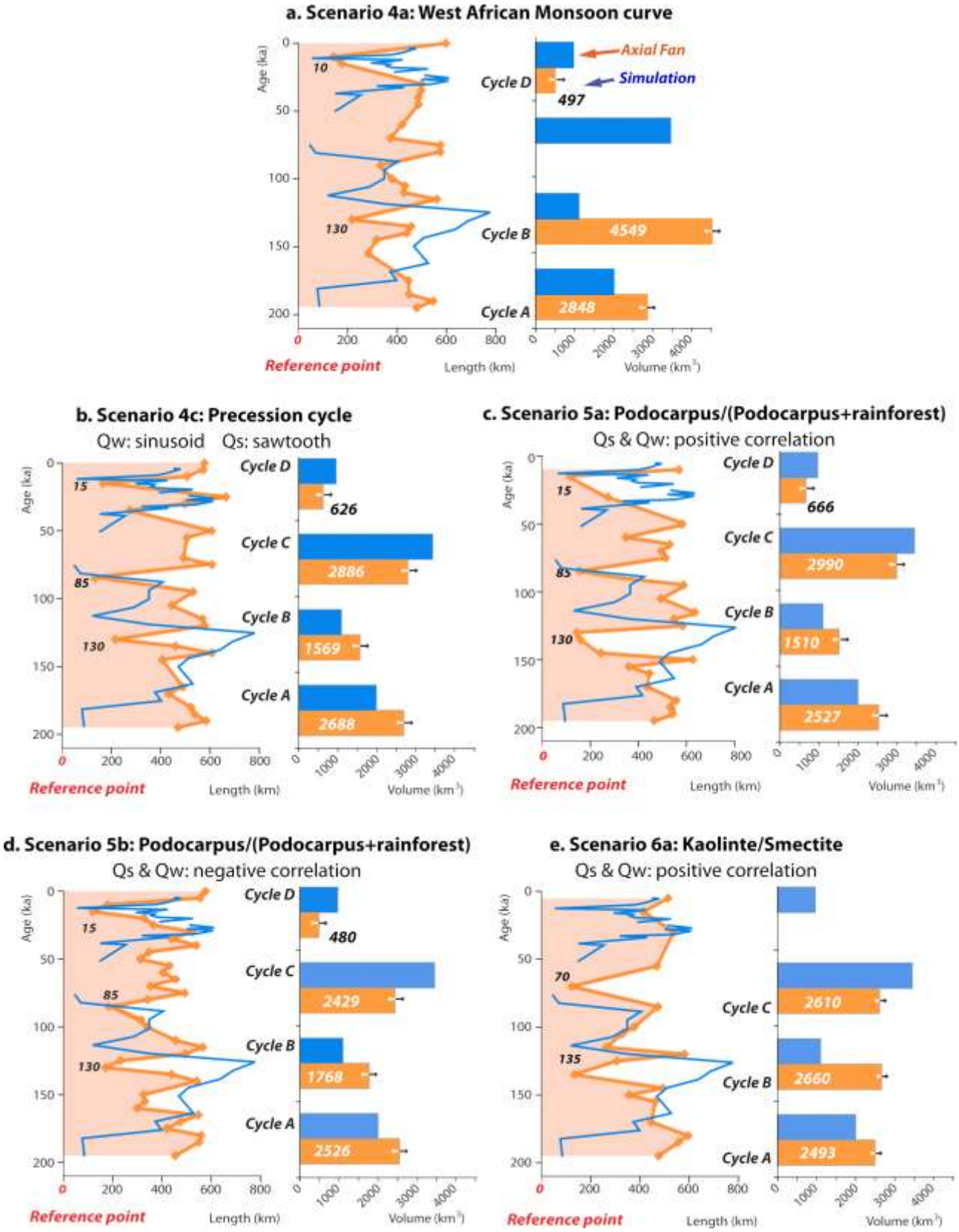

a. Scenario 4a: West African Monsoon curve
Axial Fan
Simulation
Cycle D
497
Cycle B
4549
Cycle A
2848
10
130
Age (ka)
Reference point
Length (km)
Volume (km³)
b. Scenario 4c: Precession cycle
Qw: sinusoid Qs: sawtooth
Cycle D
626
Cycle C
2886
Cycle B
1569
Cycle A
2688
15
85
130
c. Scenario 5a: Podocarpus/(Podocarpus+rainforest)
Qs & Qw: positive correlation
Cycle D
666
Cycle C
2990
Cycle B
1510
Cycle A
2527
d. Scenario 5b: Podocarpus/(Podocarpus+rainforest)
Qs & Qw: negative correlation
Cycle D
480
Cycle C
2429
Cycle B
1768
Cycle A
2526
e. Scenario 6a: Kaolinte/Smectite
Qs & Qw: positive correlation
70
135
Cycle C
2610
Cycle B
2660
Cycle A
2493

Figure 10

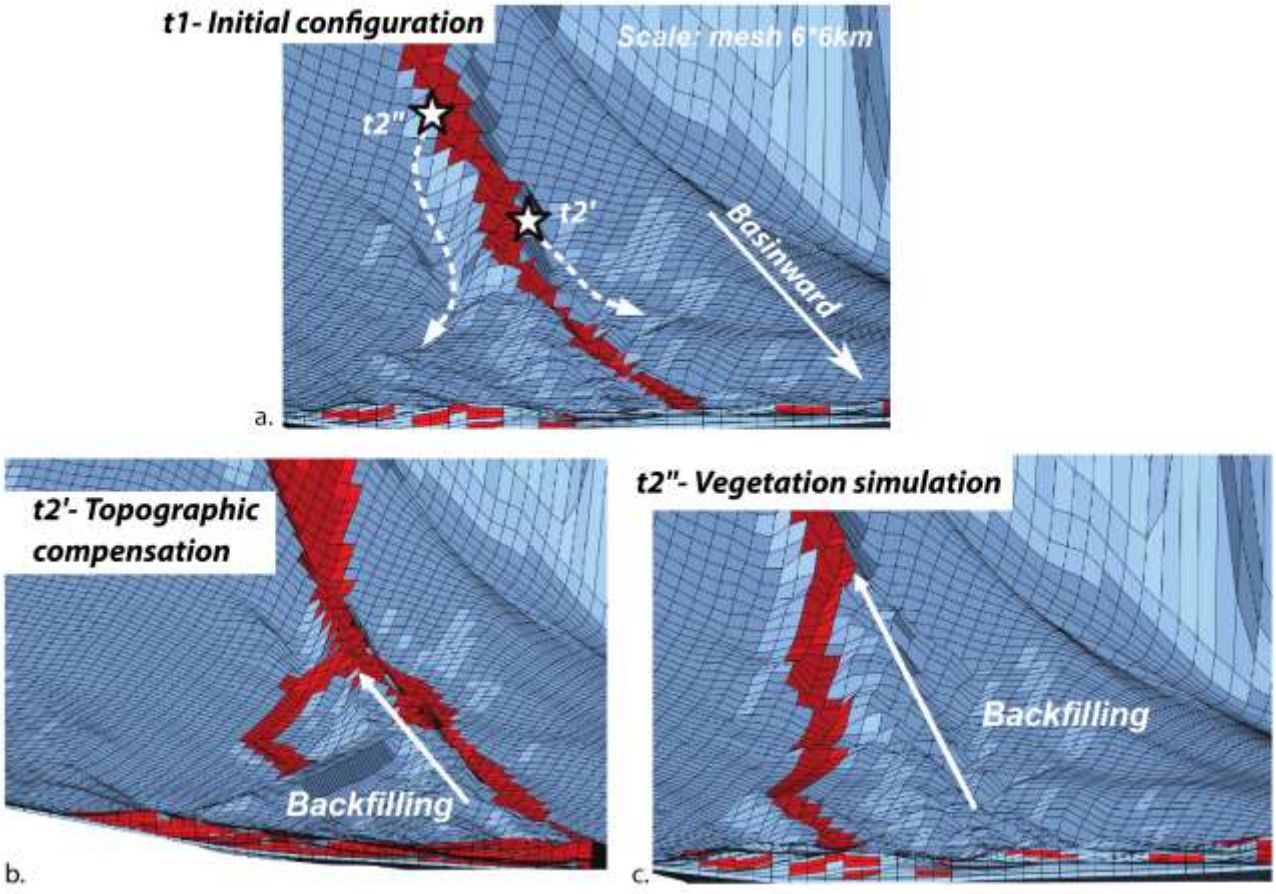

t1- Initial configuration
Scale: mesh 6*6km
t2"
t2'
Basinward
a.
t2'- Topographic compensation
Backfilling
b.
t2"- Vegetation simulation
Backfilling
c.

Figure 11

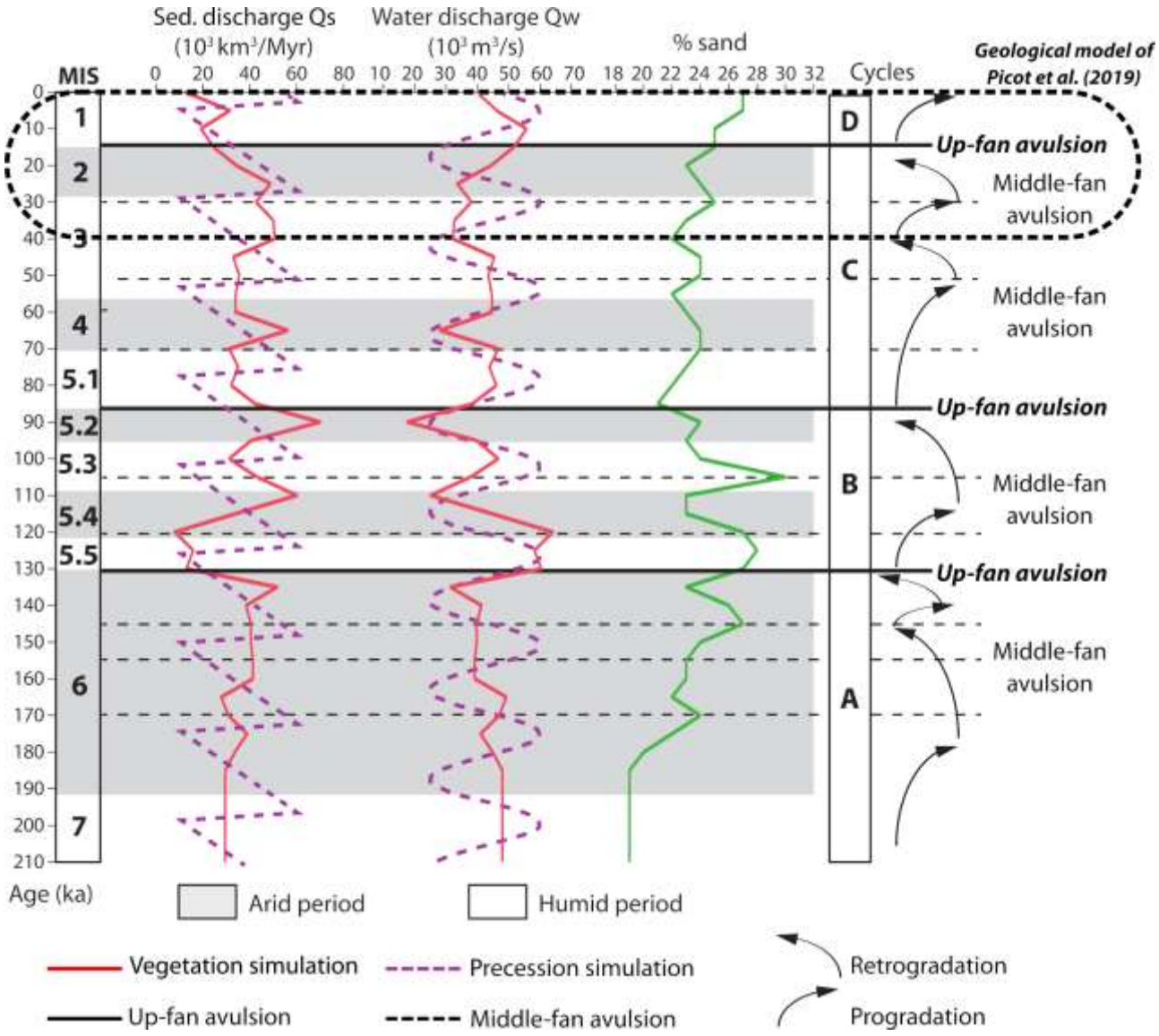

Sed. discharge Qs
(10³ km³/Myr)
Water discharge Qw
(10³ m³/s)
% sand
MIS
Cycles
Geological model of
Picot et al. (2019)
1
2
3
4
5.1
5.2
5.3
5.4
5.5
6
7
D
C
B
A
Up-fan avulsion
Middle-fan
avulsion
Up-fan avulsion
Middle-fan
avulsion
Up-fan avulsion
Middle-fan
avulsion
Age (ka)
Arid period
Humid period
Vegetation simulation
Precession simulation
Retrogradation
Up-fan avulsion
Middle-fan avulsion
Progradation

Figure 12

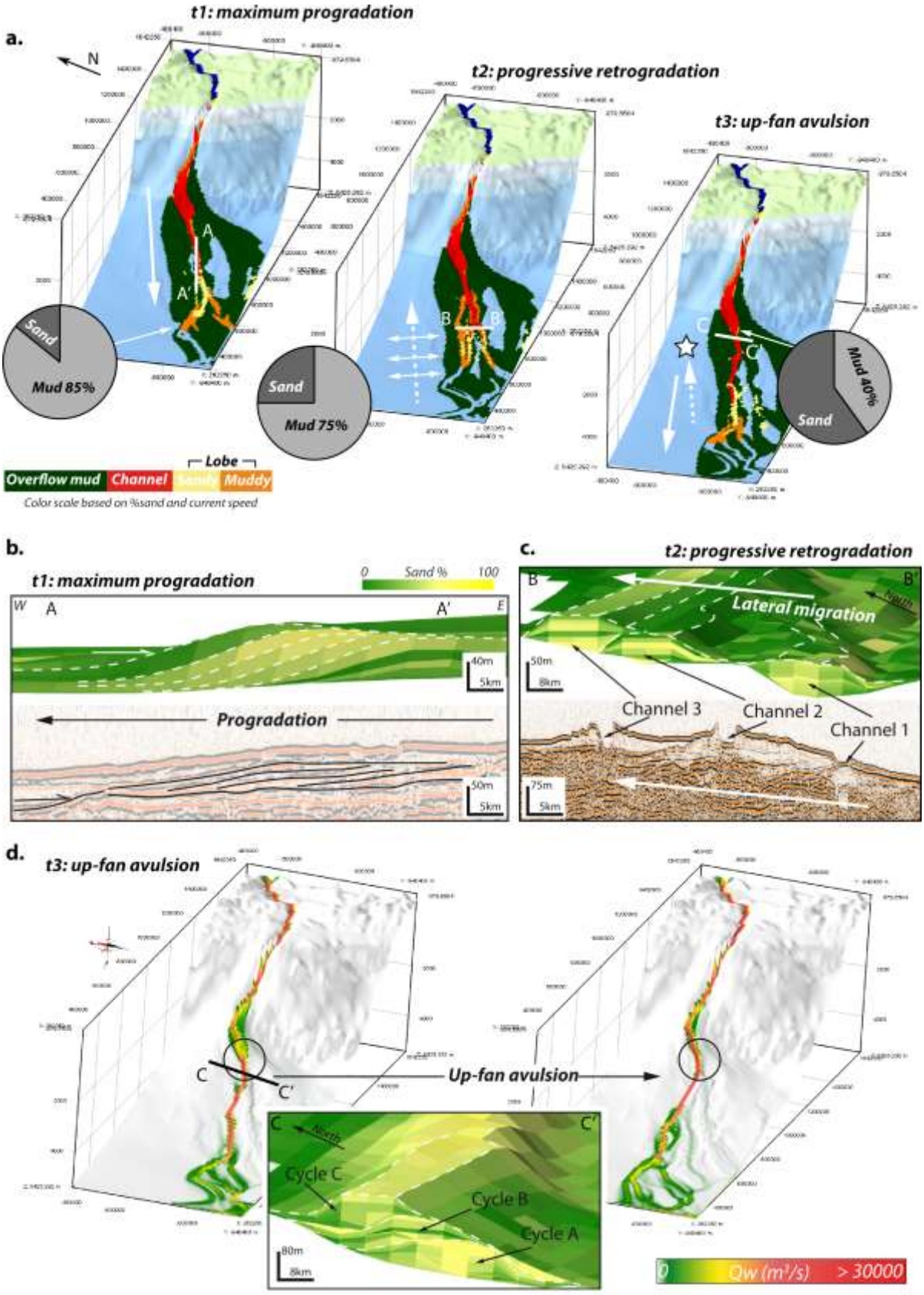

a.
t1: maximum progradation
t2: progressive retrogradation
t3: up-fan avulsion
N
A
A'
B
B'
C
C'
Sand
Mud 85%
Sand
Mud 75%
Mud 40%
Sand
Lobe
Overflow mud
Channel
Sandy
Muddy
Color scale based on %sand and current speed
b.
t1: maximum progradation
0
Sand %
100
W
A
A'
E
40m
5km
Progradation
50m
5km
c.
t2: progressive retrogradation
B
B'
North
Lateral migration
50m
8km
Channel 3
Channel 2
Channel 1
75m
5km
d.
t3: up-fan avulsion
C
C'
Up-fan avulsion
C
North
C'
Cycle C
Cycle B
Cycle A
80m
8km
0
Qw (m³/s)
> 30000

Figure 13

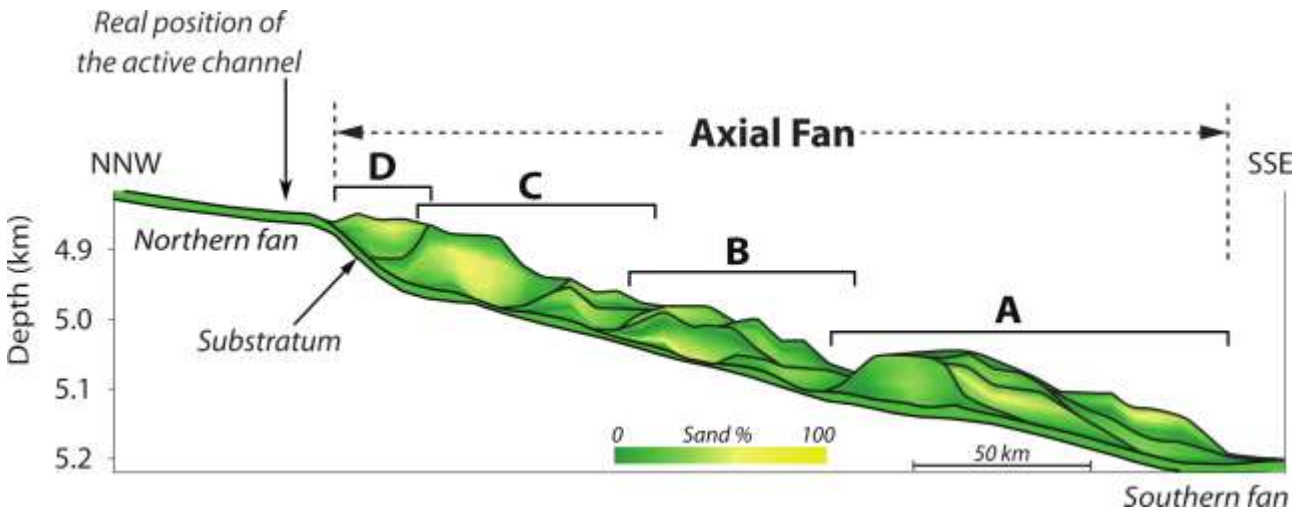

Real position of
the active channel
Axial Fan
NNW
SSE
D
C
B
A
Depth (km)
4.9
5.0
5.1
5.2
Northern fan
Substratum
0
Sand %
100
50 km
Southern fan

Figure 14